MATHEMATICS IN MEDICAL AND LIFE SCIENCES
2026, VOL. 3, NO. 1, 2733209
https://doi.org/10.1080/29937574.2026.2733209

Taylor & Francis
by informa

RESEARCH ARTICLE

OPEN ACCESS Check for updates

Mathematical modeling and optimization of monocyte-driven immune dynamics and treatment strategies in within-host *Mycobacterium tuberculosis*

Mlyashimbi Helikumi [a] and Steady Mushayabasa [b]

[a]Department of Mathematics and Statistics, College of Science and Technical Education, Mbeya University of Science and Technology, Mbeya, Tanzania; [b]Department of Mathematics and Computational Sciences, University of Zimbabwe, Harare, Zimbabwe

ABSTRACT

Tuberculosis (TB) remains a major global health challenge, driven by complex within-host interactions between *Mycobacterium tuberculosis* (Mtb) and the host immune system. To better understand these dynamics, we develop a mathematical model that incorporates monocytes, macrophages, and T lymphocytes. Analytical results show that the basic reproduction number, $\mathcal{R}_0$, depends on key infection and immune-response parameters and can exceed unity under biologically plausible conditions, leading to persistent infection. Bifurcation analysis reveals the occurrence of a backward bifurcation at $\mathcal{R}_0 = 1$, indicating that reducing $\mathcal{R}_0$ below unity may not be sufficient for disease eradication, as stable endemic equilibria can coexist with the disease-free equilibrium when $\mathcal{R}_0 < 1$. Numerical simulations under baseline parameter values demonstrate that enhancing immune response parameters substantially lowers bacterial burden, reducing bacterial populations by up to 70% within 60 days, whereas increased infection rates accelerate disease progression, doubling bacterial populations in approximately half the time. Furthermore, an optimal control analysis suggests that, under representative treatment scenarios, intensified drug treatment can reduce bacterial loads by more than 90% within 30 days; however, complete bacterial clearance may remain unattainable because of the backward bifurcation phenomenon. These findings underscore the importance of integrating immune enhancement with optimized treatment strategies and highlight that achieving $\mathcal{R}_0 < 1$ alone may not guarantee eradication of TB infection.

PLAIN LANGUAGE SUMMARY

TB remains one of the world's leading infectious diseases and is caused by the bacterium Mtb. The outcome of infection depends on complex interactions between the bacteria and the body's immune system. In this study, we developed a mathematical model to better understand how immune cells and bacteria interact during infection and how these interactions influence disease progression and treatment outcomes. Our results show that the ability of TB to persist within the body depends on both bacterial growth and the strength of the immune response. We found that improving immune function can substantially reduce bacterial levels, whereas higher infection rates can accelerate disease progression. The model also revealed a phenomenon known as backward bifurcation, meaning that reducing transmission or bacterial growth to a level traditionally considered sufficient for disease control may not always eliminate the infection. In some cases, the infection can persist even when conditions appear favorable for eradication. We further investigated the impact of drug treatment using optimal control methods. The results suggest that intensified treatment strategies can dramatically reduce bacterial burden, but complete elimination of the bacteria may still be difficult because of the complex dynamics of the infection. Overall, our findings highlight the importance of combining effective drug treatment with strategies that strengthen the immune response. Such integrated approaches may improve TB control and increase the likelihood of achieving complete bacterial clearance.

ARTICLE HISTORY
Received 23 March 2026
Revised 5 June 2026
Accepted 4 September 2026

KEYWORDS
Tuberculosis; mathematical model; monocytes; drug combination; optimal control

CONTACT Steady Mushayabasa steadymushaya@gmail.com Department of Mathematics and Computational Sciences, University of Zimbabwe, P.O. Box MP 167 Mount Pleasant, Harare, Zimbabwe

1. Introduction

Despite declines in TB incidence and mortality in some regions, the disease remains a significant global health issue, especially in resource-limited settings [1]. According to WHO, in 2024, approximately 10.7 million people contracted TB worldwide, including about 5.8 million men, 3.7 million women, and 1.2 million children [2]. TB is the leading cause of death from a single infectious agent and ranks among the top 10 causes of death globally [2].

Mtb, the causative agent of TB, has evolved sophisticated mechanisms to survive within hosts, often manipulating cell death pathways in infected macrophages to evade immune responses and antimicrobial treatments [3–5]. By altering apoptosis and necrosis timing, Mtb shields itself from immune detection and facilitates dissemination at strategic moments [5]. Enhancing therapies to better target these intracellular survival strategies is critical for improving treatment efficacy and moving toward eradication. Understanding these mechanisms will inform the development of novel therapeutic approaches, ultimately improving clinical outcomes and global TB control efforts.

Mathematical models have become invaluable tools for probing within-host disease dynamics, offering an alternative to costly and time-consuming experiments [6–24]. For example, Wigginton and Kirschner [6] used ODEs to simulate lung tissue interactions during respiratory infections, providing insights into immune regulation. Stewart et al. [24] reviewed latency modeling, emphasizing dormant bacterial states. Pedruzzi et al. [9] modeled early macrophage interactions, revealing Mtb's interference with host iron and lipid homeostasis. Despite these advances, the specific roles of monocytes and optimal drug combinations in within-host TB dynamics remain less understood. This study introduces a new model explicitly incorporating monocytes alongside other immune cells to address this gap.

Monocytes are circulating myeloid cells with short lifespans, yet they are essential in the immune response against infections. They can engulf pathogens, produce cytokines, and present antigens [25, 26]. During Mtb infection, monocytes rapidly migrate from blood to lungs, differentiating into monocyte-derived macrophages (MDMs) that help contain the bacteria [25–28]. Despite their importance, monocytes are often underrepresented or omitted in existing TB models, limiting their accuracy in capturing immune complexity.

Beyond modeling monocyte dynamics, this work focuses on identifying optimal drug combinations to control Mtb. Standard TB treatments (RIPE: Rifampicin, Isoniazid, Pyrazinamide, Ethambutol) aim to rapidly reduce bacterial load, sterilize tissues, prevent resistance, and target dormant bacteria [29–31]. However, suboptimal drug performance can lead to persistence or tolerance [32]. Quantitatively evaluating combination therapies' potential to overcome persistence is thus essential. We develop a within-host Mtb model based on recent literature [16–18]. The model is analyzed via the basic reproduction number ($\mathcal{R}_0$) and bifurcation analysis, revealing a backward bifurcation at $\mathcal{R}_0 = 1$. An optimal control problem is formulated with controls representing drug administration efforts, aiming to minimize bacterial and infected cell populations. This work is among the first to assess drug combination optimization in the context of monocyte involvement, providing insights into immune and treatment strategies to improve outcomes.

The paper is organized as follows: Section 2.1 formulates the model, computes $\mathcal{R}_0$, and analyzes stability; the model is extended into an optimal control problem with its optimality system derived. Section 3 presents numerical results and discussion. Conclusions highlight key findings, limitations, and future directions.

2. Methods and results

2.1. Model derivation

A system of nonlinear ordinary differential equations (NODEs) is proposed to describe the interactions among the Mtb pathogen, monocytes, macrophages, and T lymphocytes within the lung environment. When monocytes are recruited into lung tissue, they differentiate into MDMs [27, 28]. To facilitate this, the variables in the model are defined as follows: M_0 represents uninfected monocytes, M_i represents infected monocytes, D_{mu} denotes uninfected MDMs, D_{mi} corresponds to infected MDMs, R_{mu} signifies uninfected resident macrophages, R_{mi} indicates infected resident macrophages, B models the population of Mtb, and T represents T lymphocytes. The model is built upon several key assumptions, outlined below:

- *Recruitment, differentiation and infection of monocytes*: Circulating blood monocytes are recruited to the lungs, especially during injury, infection, or inflammation. Once in the lung tissue, they differentiate into MDMs, which are essential for immune defense and tissue repair [27]. These circulating monocytes are short-lived, with an estimated half-life of approximately 1 to 3 days, significantly shorter than that of resident macrophages [28]. Previous studies suggest that monocytes may encounter soluble products of Mtb, leading to their infection before completing the differentiation process [33].
- *Interaction of Mtb with RAMs*: When aerosolized Mtb enters the lungs, it first encounters RAMs, which are critical components of the innate immune response. These RAMs become infected upon contact with Mtb, either via phagocytosis or other mechanisms [34]. This interaction triggers recognition through pattern recognition receptors (PRRs), such as Toll-like receptors (TLRs), leading to the production of cytokines and chemokines that recruit additional immune cells. These early immune responses are vital for containing the infection, activating adaptive immunity, and orchestrating a coordinated defense involving various immune mediators [34, 35].
- *Dynamics of RAMs*: RAMs are among the first cells to encounter Mtb upon infection [34]. When uninfected RAMs come into contact with Mtb, they become infected, initiating a cascade of immune responses. The interaction between Mtb and macrophages triggers complex immune mechanisms that work together to mount an effective defense against the pathogen [35].
- *Population decline and bacterial proliferation*: Over time, the populations of both uninfected and infected RAMs decline primarily due to natural cell death processes [23]. Additionally, infected RAMs decrease as a result of immune-mediated clearance mechanisms [16]. Despite this decline, a certain fraction of alveolar macrophages contributes to the proliferation of Mtb, thereby increasing the bacterial load within the host.

Based on these assumptions, the dynamics of uninfected macrophages are approximated by the following system of equations. (A summary of the model variables and their biological definitions is provided in Table 1, and the model transition diagram is in Figure 1.):

$$\frac{dM_o}{dt} = s_0 - (\phi_0 + \phi_1)M_o - \beta_0 B M_o, \tag{1}$$

$$\frac{dM_i}{dt} = \beta_0 B M_o - (\alpha_0 + \alpha_1)M_i - \frac{\gamma M_i T}{a_0 + T}, \tag{2}$$

$$\frac{dD_{mu}}{dt} = \phi_1 M_o - \beta_1 B D_{mu} - \mu_0 D_{mu}, \tag{3}$$

$$\frac{dD_{mi}}{dt} = \alpha_1 M_i + \beta_1 B D_{mu} - \mu_1 D_{mi} - \frac{\gamma D_{mi} T}{a_1 + T}, \tag{4}$$

$$\frac{dR_{mu}}{dt} = s_1 - \beta_2 B R_{mu} - \mu_2 R_{mu}, \tag{5}$$

$$\frac{dR_{mi}}{dt} = \beta_2 B R_{mu} - b R_{mi} - \frac{\gamma R_{mi} T}{a_2 + T}, \tag{6}$$

$$\begin{aligned}\frac{dB}{dt} = {} & \delta B\left(1 - \frac{B}{K}\right) + \alpha_0 N_0 M_i + \frac{N_1 \gamma M_i T}{a_0 + T} + N_2 \mu_1 D_{mi} + \frac{N_3 \gamma D_{mi} T}{a_1 + T} + N_4 b R_{mi} \\ & + \frac{N_5 \gamma R_{mi} T}{a_2 + T} - (\eta_0 + H_0\beta_0)B M_o - (\eta_1 + H_1\beta_1)B D_{mu} - (\eta_2 + H_2\beta_2)B R_{mu},\end{aligned} \tag{7}$$

$$\frac{dT}{dt} = s_3 + \frac{c_0 M_i T}{1 + e_0 T} + \frac{c_1 D_{mi} T}{1 + e_1 T} + \frac{c_2 R_{mi} T}{1 + e_2 T} + \frac{c_3 B T}{1 + e_3 T} - \sigma T, \tag{8}$$

with initial conditions:

$$\begin{aligned} & M_o(0) = M_{o0} \geq 0, \quad M_i(0) = M_{i0} \geq 0, \quad D_{mu}(0) = D_{mu0} \geq 0, \quad D_{mi}(0) = D_{mi0} \geq 0, \\ & R_{mu}(0) = R_{mu0} \geq 0, \quad R_{mi}(0) = R_{mi0} \geq 0, \quad B(0) = B_0 \geq 0, \quad T(0) = T_0 \geq 0. \end{aligned} \tag{9}$$

- The first equation describes the dynamics of uninfected monocytes recruited into the lung environment.

Table 1. Summary of variables in the model (1)–(8).

Variable	Biological definition	Variable	Biological definition
$M_o(t)$	Uninfected monocytes	$M_i(t)$	Infected monocytes
$D_{mu}(t)$	Uninfected MDMs	$D_{mi}(t)$	Infected MDMs
$R_{mu}(t)$	Uninfected RAMs	$R_{mi}(t)$	Infected RAMs
$B(t)$	Population of Mtb	$T(t)$	Population of T lymphocytes

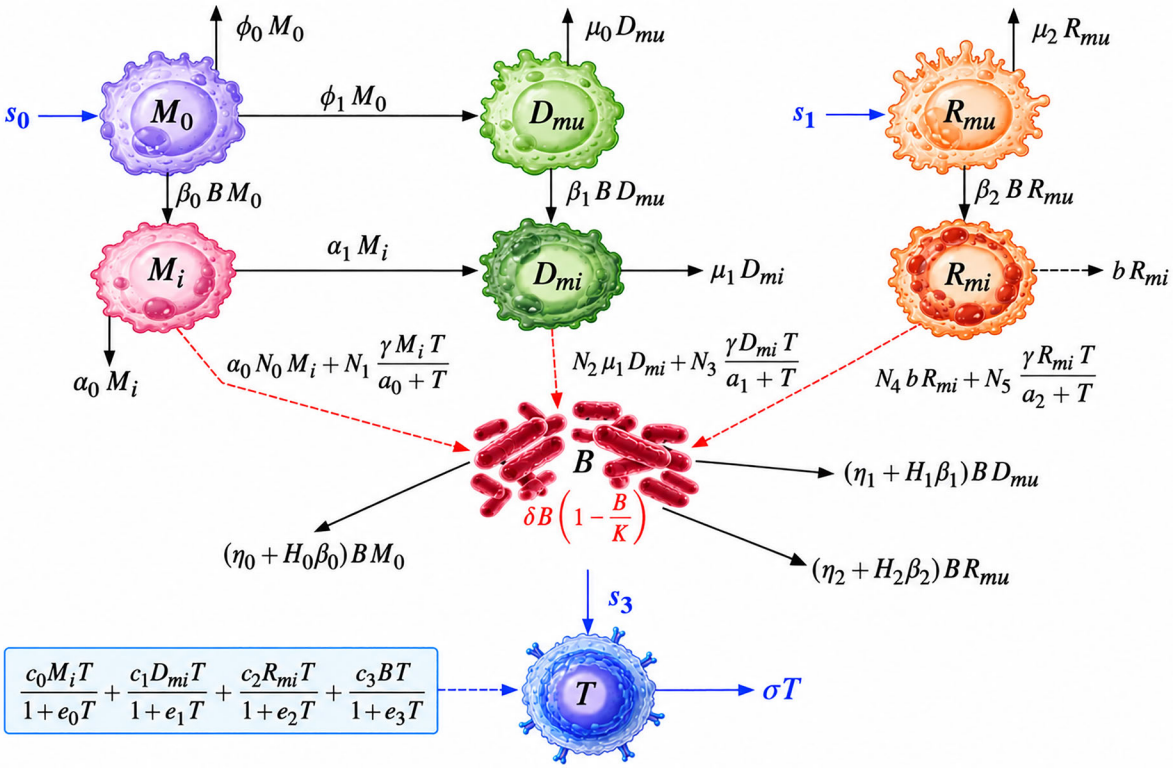

Figure 1. Model flow diagram illustrating the interactions between Mtb and the host immune system, including key cellular components, pathogen-host interactions, and immune responses modeled in the system (Equations (1)–(8)).

Uninfected monocytes are recruited into the lung tissue at a constant rate s_0, and they undergo natural death at rate ϕ_0. Once in the tissue, monocytes differentiate into uninfected MDMs at rate ϕ_1. Additionally, monocytes can become infected by bacteria before differentiating into MDMs at infection rate β_0.

- The second equation accounts for the dynamics of infected monocytes prior to differentiation. This population increases through infection of susceptible monocytes at rate β_0. It decreases through natural death at rate α_0, differentiation into MDMs at rate α, and clearance by T-cells modeled by the function $\frac{\gamma M_i T}{a_0+T}$, where γ represent the cell-mediated immune response, and a_0 is the the saturation constant representing the T-cell concentration at which the lysis rate is half-maximal.
- The third equation represents the dynamics of susceptible MDMs. This population increases through the differentiation of uninfected monocytes. It decreases due to infection by Mtb pathogen, at rate β_1, as well as natural death, at rate μ_0.
- The fourth equation accounts for the dynamics of infected MDMs population, which increases through infection of susceptible MDMs and the conversion of infected monocytes, with parameter α_1 accounting for the conversion rate. Infected MDMs decrease due to natural death at rate μ_1. Additionally, infected MDMs are subject to T-cell-mediated lysis, modeled with a Michaelis-Menten term $\frac{\gamma D_{mi} T}{a_1+T}$, where γ is the maximum lysis rate, and a_1 is the saturation constant representing the T-cell concentration at which the lysis rate is half-maximal.
- The fifth equation represent the concentration of uninfected RAMs. This population increases at a constant rate s_1, and it decreases through infection by the bacteria B at rate β_2, as well as through natural death at

rate μ_2. Infected RAMs are produced when susceptible RAMs become infected, and they decrease due to natural death at rate b. Additionally, infected resident macrophages are removed by T-cells, and this process is modeled by a Michaelis-Menten term $\frac{\gamma R_{mi} T}{a_2+T}$, where γ is the maximum lysis rate, and a_1 is the saturation constant representing the T-cell concentration at which the lysis rate is half-maximal.

- The bacterial population proliferates logistically at rate δ, with a maximum capacity K. Bacteria are released from infected MDMs and RAMs, with contributions $N_0, N_1, N_2, N_3, N_4, N_5$ representing the number of bacteria released per infected cell type. Bacteria are cleared through immune responses involving monocytes, macrophages, and RAMs, each contributing to bacterial killing at rates η_0, η_1, η_2 respectively, modulated by immune enhancement factors H_0, H_1, H_2.
- The T-cell population is produced at a baseline rate s_3. T-cells are activated proportionally to the presence of infected macrophages, MDMs, RAMs, and bacteria, with activation rates c_0, c_1, c_2, c_3, and maximum activation levels e_0, e_1, e_2, e_3. These parameters model the immune system's capacity to respond under different pathogen loads. The activation follows Michaelis-Menten dynamics, where the saturation constants e_0, e_1, e_2, e_3 represent the T-cell concentration at which activation is half-maximal. T-cells decay at rate σ.

2.2. Basic properties of the model

To demonstrate that the solutions of (1)–(8) are well-posed and bounded for all time, we start by showing that, given any non-negative initial conditions (9), the solutions will remain positive. From the first, second, and third equations of model (1), we have: $\frac{dM_o}{dt}|_{M_o=0} = s_0 > 0$, $\frac{dM_i}{dt}|_{M_i=0} = \beta_0 B M_o > 0$, and $\frac{dD_{mu}}{dt}|_{D_{mu}=0} = \phi_1 M_o$, $\frac{dD_{mi}}{dt}|_{D_{mi}=0} = \alpha_1 M_i > 0$, $\frac{dR_{mu}}{dt}|_{R_{mu}=0} = s_1 > 0$, and $\frac{dR_{mi}}{dt}|_{R_{mi}=0} = \beta_2 B R_{mu} > 0$, respectively. Similarly, from the remaining equations of model (1), we have:

$$\begin{aligned} \left.\frac{dB}{dt}\right|_{B=0} &= \alpha_0 N_0 M_i + \frac{N_1 \gamma M_i T}{a_0 + T} + N_2 \mu_1 D_{mi} + \frac{N_3 \gamma D_{mi} T}{a_1 + T} + N_4 b R_{mi} + \frac{N_5 \gamma R_{mi} T}{a_2 + T} > 0, \\ \left.\frac{dT}{dt}\right|_{T=0} &= s_3 > 0. \end{aligned} \tag{10}$$

Therefore, we conclude that, given any non-negative initial conditions (9), the solutions will remain positive for all time. Consequently, the vector field defined by the right-hand side of model (1)–(8) on each coordinate plane is either tangent to the plane or points inward toward the interior of $\mathbb{R}^7_+$. Hence, the domain $\mathbb{R}^7_+$ is positively invariant.

2.3. Basic reproduction number

The reproduction number $\mathcal{R}_0$, is an important metric for epidemiological models since it determines the strength of the disease to persist. If $\mathcal{R}_0 > 1$, it signals persistence of infection within a single host, and $\mathcal{R}_0 < 1$, implies the disease dies out. To determine $\mathcal{R}_0$, we follow the next generation method (NGM) [36, 37]. The first step in determining $\mathcal{R}_0$ entails computing the disease-free equilibrium (DFE) point of the system. Through direct calculations, one can easily verify that system (1)–(8) admits the DFE $\mathcal{E}^* = (M_o^*, 0, D_{mu}^*, 0, R_{mu}^*, 0, 0, T^*)$, with:

$$M_o^* = \frac{s_0}{\phi_0 + \phi_1}, \quad D_{mu}^* = \frac{s_0 \phi_1}{\mu_0(\phi_0 + \phi_1)} \quad R_{mu}^* = \frac{s_1}{\mu_2}, \quad T^* = \frac{s_3}{\sigma}.$$

Next, we define the relevant vectors, focusing on the infected compartments which are capable of generating secondary infections, that is, M_i, D_{mi}, R_{mi}, B. Thus, the matrix $\mathcal{F}$ representing terms that account for the generation of new infection and the non-singular matrix $\mathcal{V}$ denoting the remaining transfer terms, evaluated at the

disease-free equilibrium, are respectively given by:

$$\mathcal{F} = \begin{bmatrix} 0 & 0 & 0 & \frac{\beta_0 s_0}{\phi_0+\phi_1} \\ 0 & 0 & 0 & \frac{\beta_1 s_0 \phi_1}{\mu_0(\phi_0+\phi_1)} \\ 0 & 0 & 0 & \frac{\beta_2 s_1}{\mu_2} \\ \alpha_0 N_0 + \frac{N_1 \gamma s_3}{a_0\sigma + s_3} & N_2\mu_1 + \frac{N_3 \gamma s_3}{a_1\sigma + s_3} & N_4 b + \frac{N_5 \gamma s_3}{a_2\sigma + s_3} & \delta \end{bmatrix},$$

$$\mathcal{V} = \begin{bmatrix} \alpha_0 + \alpha_1 + \frac{\gamma s_3}{a_0\sigma + s_3} & 0 & 0 & 0 \\ -\alpha_1 & \mu_1 + \frac{\gamma s_3}{a_1\sigma + s_3} & 0 & 0 \\ 0 & 0 & b + \frac{\gamma s_3}{a_2\sigma + s_3} & 0 \\ 0 & 0 & 0 & \mathcal{Q}_0 \end{bmatrix}, \tag{11}$$

with:

$$\mathcal{Q}_0 = \frac{(\eta_0 + H_0\beta_0)s_0}{\phi_0+\phi_1} + \frac{(\eta_1 + H_1\beta_1)s_0\phi_1}{\mu_0(\phi_0+\phi_1)} + \frac{(\eta_2 + H_2\beta_2)s_1}{\mu_2}.$$

It follows that the reproduction number of model (1)–(8) is:

$$\mathcal{R}_0 = \rho(\mathcal{F}\mathcal{V}^{-1}) = \frac{1}{2}\left(\mathcal{Q}_1 + \sqrt{\mathcal{Q}_1^2 + 4(\mathcal{Q}_2\mathcal{Q}_3 + \mathcal{Q}_4\mathcal{Q}_5 + \mathcal{Q}_6\mathcal{Q}_7)}\right),$$

$$\mathcal{Q}_1 = \frac{\delta}{\mathcal{Q}_0}, \quad \mathcal{Q}_2 = \frac{\beta_0 s_0}{\mathcal{Q}_0(\phi_0+\phi_1)}, \quad \mathcal{Q}_3 = \frac{\alpha_0 N_0 + \frac{N_1\gamma s_3}{a_0\sigma+s_3}}{\alpha_0+\alpha_1+\frac{\gamma s_3}{a_0\sigma+s_3}} + \alpha_1 \frac{N_2\mu_1 + \frac{N_3\gamma s_3}{a_1\sigma+s_3}}{(\alpha_0+\alpha_1+\frac{\gamma s_3}{a_0\sigma+s_3})(\mu_1+\frac{\gamma s_3}{a_1\sigma+s_3})}, \tag{12}$$

$$\mathcal{Q}_4 = \frac{\beta_1 s_0 \phi_1}{\mathcal{Q}_0\mu_0(\phi_0+\phi_1)}, \quad \mathcal{Q}_5 = \frac{N_2\mu_1 + \frac{N_3\gamma s_3}{a_1\sigma+s_3}}{\mu_1+\frac{\gamma s_3}{a_1\sigma+s_3}}, \quad \mathcal{Q}_6 = \frac{\beta_2 s_1}{\mu_2\mathcal{Q}_0}, \quad \mathcal{Q}_7 = \frac{N_4 b + \frac{N_5\gamma s_3}{a_2\sigma+s_3}}{b+\frac{\gamma s_3}{a_2\sigma+s_3}}.$$

2.4. Stability analysis of the disease-free equilibrium

Our goal in this section is to perform a stability analysis of the DFE. We will begin by analyzing the local stability of the system, which involves examining the eigenvalues of the Jacobian matrix evaluated at the DFE. Following this, we will proceed to assess the global stability of the equilibrium by closely following the approach outlined in Castillo-Chavez [38]. Linearizing the model (Equations (1)–(8)) around the equilibrium point $\mathcal{E}^0$ yields:

$$J = \begin{bmatrix} -(\phi_0+\phi_1) & 0 & 0 & 0 & 0 & 0 & -J_0 & 0 \\ 0 & -J_1 & 0 & 0 & 0 & 0 & J_0 & 0 \\ \phi_1 & 0 & -\mu_0 & 0 & 0 & 0 & -J_2 & 0 \\ 0 & \alpha_1 & 0 & -J_3 & 0 & 0 & J_2 & 0 \\ 0 & 0 & 0 & 0 & -\mu_2 & 0 & -J_4 & 0 \\ 0 & 0 & 0 & 0 & 0 & -J_5 & J_4 & 0 \\ 0 & J_6 & 0 & J_7 & 0 & J_8 & \delta - \mathcal{Q}_0 & 0 \\ 0 & J_9 & 0 & J_{10} & 0 & J_{11} & J_{12} & -\sigma. \end{bmatrix}, \tag{13}$$

where

$$J_0 = \frac{\beta_0 s_0}{\phi_0+\phi_1}, \quad J_1 = \left(\alpha_0+\alpha_1+\frac{\gamma s_3}{a_0\sigma+s_3}\right), \quad J_2 = \frac{\beta_1 s_0\phi_1}{\mu_0(\phi_0+\phi_1)}, \quad J_3 = \left(\mu_1+\frac{\gamma s_3}{a_1\sigma+s_3}\right),$$

$$J_4 = \frac{\beta_2 s_1}{\mu_2}, \quad J_5 = \left(b+\frac{\gamma s_3}{a_2\sigma+s_3}\right), \quad J_6 = \alpha_0 N_0 + \frac{N_1\gamma s_3}{a_0\sigma+s_3}, \quad J_7 = N_2\mu_1 + \frac{N_3\gamma s_3}{a_1\sigma+s_3},$$

$$J_8 = N_4 b + \frac{N_5\gamma s_3}{a_2\sigma+s_3}, \quad J_9 = \frac{c_0 s_3}{\sigma+e_0 s_3}, \quad J_{10} = \frac{c_1 s_3}{\sigma+e_1 s_3}, \quad J_{11} = \frac{c_2 s_3}{\sigma+e_2 s_3}, \quad J_{12} = \frac{c_3 s_3}{\sigma+e_3 s_3}.$$

Notably, the eigenvalues $-\sigma$, $-\mu_2$, $-\mu_0$, and $-(\phi_0+\phi_1)$ are associated with the diagonal entries of J. Therefore, the matrix J can be reduced to a 4×4 matrix, focusing on the subspace relevant for stability analysis:

$$\tilde{J}=\begin{bmatrix} -J_1 & 0 & 0 & J_0 \\ \alpha_1 & -J_3 & 0 & J_2 \\ 0 & 0 & -J_5 & J_4 \\ J_6 & J_7 & J_8 & \delta-\mathcal{Q}_0 \end{bmatrix}. \tag{14}$$

Observe that $\tilde{J}=F-V$, where matrices F and V are defined as in Equation (11). The basic reproduction number $\mathcal{R}_0$ is identified as the dominant eigenvalue of the next-generation matrix $F-V$. Consequently, we conclude that the DFE $\mathcal{E}^0$ is locally asymptotically stable if $\mathcal{R}_0<1$, and unstable otherwise. This leads to the formal result:

Theorem 2.1: *If $\mathcal{R}_0<1$, the DFE $\mathcal{E}^0$ is locally asymptotically stable, otherwise it is unstable.*

Now, we proceed to investigate the global stability of $\mathcal{E}^0$. By closely following the approach in Castillo-Chavez [38], let $X=(M_o,D_{mu},R_{mu},T^{)}\in\mathbb{R}^4_+$ be the number of uninfected cells, and $Y=(M_i,D_{mi},R_{mi},B)\in\mathbb{R}^4_+$ be the number of infected cells and bacterial population. It follows that model (1)–(8) can be rewritten as Equation (15):

$$\begin{aligned} X'(t)&=F(X,Y),\\ Y'(t)&=G(X,Y),\quad G(X,\mathbf{0})=0. \end{aligned} \tag{15}$$

According to Castillo-Chavez [38], if the following conditions holds, then $\mathcal{E}^0$ is said to be globally asymptotically stable:

H1 : For $X'(t)=F(X,\mathbf{0})\geq 0$, X is globally asymptotically stable, H2 : $G(X,Y)=UY-\tilde{G}(X,Y)$, $\tilde{G}(X,Y)\geq 0$,

where U is defined in Equation (14). For condition (H1), we have:

$$F(X,\mathbf{0})=\begin{bmatrix} (\phi_0+\phi_1)\left(\dfrac{s_0}{(\phi_0+\phi_1)}-M_o\right) \\ \mu_0\left(\dfrac{s_0\phi_1}{\mu_0(\phi_0+\phi_1)}-D_{mu}\right) \\ \mu 2\left(\dfrac{s_1}{\mu_2}-R_{mu}\right) \\ \sigma\left(\dfrac{s_3}{\sigma}-T\right) \end{bmatrix}. \tag{16}$$

Since $M_o(t)\leq M^*=\frac{s_0}{\phi_0+\phi_1}$, $D_{mu}(t)\leq D^*_{mu}=\frac{s_0\phi_1}{\mu_0(\phi_0+\phi_1)}$, $R_{mu}(t)\leq R^*_{mu}=\frac{s_1}{\mu_2}$ and $T(t)\leq T^*=\frac{s_3}{\sigma}$, for all $t\geq 0$ it follows that $F(X,\mathbf{0})\geq 0$. For condition (H2), it can be readily verified that:

$$\tilde{G}(X,Y)=\begin{bmatrix} \tilde{G}_1(X,Y) \\ \tilde{G}_2(X,Y) \\ \tilde{G}_3(X,Y) \\ \tilde{G}_4(X,Y) \end{bmatrix}, \tag{17}$$

where

$$\tilde{G}_1(X,Y) = \beta_0 B\left(M_o^* - M_o\right) - \gamma\left(\frac{T^*}{a_0+T^*} - \frac{T}{a_0+T}\right)M_i,$$
$$\tilde{G}_2(X,Y) = \beta_1 B\left(D_{mu}^* - D_{mu}\right) - \gamma\left(\frac{T^*}{a_1+T^*} - \frac{T}{a_1+T}\right)D_{mi},$$
$$\tilde{G}_3(X,Y) = \beta_2 B\left(R_{mu}^* - R_{mu}\right) - \gamma\left(\frac{T^*}{a_2+T^*} - \frac{T}{a_2+T}\right)R_{mi},$$
$$\begin{aligned}\tilde{G}_4(X,Y) = &-(\beta_0 H_0 + \eta_0)\left(M_o^* - M_o\right)B + N_1\gamma\left(\frac{T^*}{a_0+T^*} - \frac{T}{a_0+T}\right)M_i\\ &-(\beta_1 H_1 + \eta_1)\left(D_{mu}^* - D_{mu}\right)B + N_3\gamma\left(\frac{T^*}{a_1+T^*} - \frac{T}{a_1+T}\right)D_{mi}\\ &-(\beta_2 H_2 + \eta_2)\left(R_{mu}^* - R_{mu}\right)B + N_5\gamma\left(\frac{T^*}{a_2+T^*} - \frac{T}{a_2+T}\right)R_{mi}.\end{aligned}$$

Since $T(t) \le T^*$, it follows that, $\frac{T}{a_i+T} \le \frac{T^*}{a_i+T^*}$, $i = 0, 1, 2$, which implies that $\tilde{G}_1(X,Y)$, $\tilde{G}_2(X,Y)$, and $\tilde{G}_3(X,Y)$ may not be greater than or equal to zero for all time. Additionally, $\tilde{G}_4(X,Y)$ contains negative terms, and as such, it may also not be non-negative for all time. This outcome suggests that the disease-free equilibrium $\mathcal{E}^0$ is unlikely to be globally asymptotically stable when $\mathcal{R}_0 < 1$. There exists the possibility that both the DFE and EE points coexist. Consequently, we arrive at the following result.

Theorem 2.2: *If $\mathcal{R}_0 < 1$, then the disease-free equilibrium $\mathcal{E}^0$ is not globally asymptotically stable.*

2.5. Bifurcation analysis

According to Theorem 2.2, there is a possibility that both the DFE and endemic equilibrium (EE) points coexist. To investigate this likelihood, we perform bifurcation analysis. Without loss of generality, for this analysis, we consider a simplified version of models (1)–(8). Du et al. [17] refer to previous work [6–8] and note that, in Equations (1)–(7), the action of cytotoxic T lymphocytes (CTLs) is proportional to the CD4 T-cell effector function – the ratio of the total number of CD4 T-cells to the total number of target cells $(T(t)/j)$, where $j = M_i(t), D_{mi}(t), R_{mi}(t)$. This suggests that the asymptotic behavior of the immune response can be described as either $T(t)/j \ll a_k$ or $T(t)/j \gg a_k$, with a_k representing the corresponding saturation constant of the variable j. Consequently, the infected cell killing term $\frac{\gamma jT}{a_k+T}$ can be simplified to $\gamma^* j$, where $\gamma^* \in \{0, \gamma\}$. This reduction allows us to simplify models (1)–(8) to the reduced form (18)–(24):

$$M_o'(t) = s_0 - (\phi_0 + \phi_1)M_o - \beta_0 B M_o, \tag{18}$$
$$M_i'(t) = \beta_0 B M_o - (\alpha_0 + \alpha_1)M_i - \gamma^* M_i, \tag{19}$$
$$D_{mu}'(t) = \phi_1 M_o - \beta_1 B D_{mu} - \mu_0 D_{mu}, \tag{20}$$
$$D_{mi}'(t) = \alpha_1 M_i + \beta_1 B D_{mu} - \mu_1 D_{mi} - \gamma^* D_{mi}, \tag{21}$$
$$R_{mu}'(t) = s_1 - \beta_2 B R_{mu} - \mu_2 R_{mu}, \tag{22}$$
$$R_{mi}'(t) = \beta_2 B R_{mu} - b R_{mi} - \gamma^* R_{mi}, \tag{23}$$
$$\begin{aligned}B'(t) = &\delta B\left(1 - \frac{B}{K}\right) + \alpha_0 N_0 M_i + N_1\gamma^* M_i + N_2\mu_1 D_{mi} + N_3\gamma^* D_{mi}\\ &+ N_4 b R_{mi} + N_5\gamma^* R_{mi} - (\eta_0 + H_0\beta_0)B M_o - (\eta_1 + H_1\beta_1)B D_{mu}\\ &- (\eta_2 + H_2\beta_2)B R_{mu},\end{aligned} \tag{24}$$

Denote $\hat{\mathcal{E}} = (\hat{M}_o, \hat{M}_i, \hat{D}_{mu}, \hat{D}_{mi}, \hat{R}_{mu}, \hat{R}_{mi}, \hat{B})$ as an arbitrary endemic equilibrium of Equation (18)–(24). At steady state $\hat{\mathcal{E}}$ we have:

$$\begin{aligned}
\hat{M}_o(\hat{B}) &= \frac{s_0}{n_0 + \beta_0 \hat{B}}, \quad \hat{M}_i(\hat{B}) = \frac{\beta_0 s_0 \hat{B}}{n_1(n_0 + \beta_0 \hat{B})}, \quad \hat{D}_{mu}(\hat{B}) = \frac{\phi_1 s_0}{(\beta_1 \hat{B} + \mu_0)(n_0 + \beta_0 \hat{B})}, \\
\hat{D}_{mi}(\hat{B}) &= \frac{1}{n_2}\left[\frac{\alpha_1 \beta_0 \hat{B} s_0}{n_1(n_0 + \beta_0 \hat{B})} + \frac{\beta_1 \hat{B} \phi_1 s_0}{(n_0 + \beta_0 \hat{B})(\beta_1 \hat{B} + \mu_0)}\right], \quad \hat{R}_{mu}(\hat{B}) = \frac{s_1}{\beta_2 \hat{B} + \mu_2}, \\
\hat{R}_{mi}(\hat{B}) &= \frac{\beta_2 s_1 \hat{B}}{n_3(\beta_2 \hat{B} + \mu_2)},
\end{aligned} \tag{25}$$

with

$$n_0 = (\phi_0 + \phi_1), \quad n_1 = (\alpha_0 + \alpha_1 + \gamma^*), \quad n_2 = (\mu_1 + \gamma^*), \quad n_3 = (b + \gamma^*).$$

Substituting $\hat{M}_o$, $\hat{M}_i$, $\hat{D}_{mu}$, $\hat{D}_{mi}$, $\hat{R}_{mu}$, and $\hat{R}_{mi}$ into Equation (23) yields

$$g(\hat{B}) = \bar{a}_4 \hat{B}^4 + \bar{a}_3 \hat{B}^3 + \bar{a}_2 \hat{B}^2 + \bar{a}_1 \hat{B} + \bar{a}_0, \tag{26}$$

where $\bar{a}_m$, $m = 0,1,2,3,4$, are constants. The full expressions for a_m are extremely lengthy, making it difficult to draw conclusions. Nevertheless, the system (18)–(24) can be further condensed by grouping cells based on infection status and summing them up. Thus, one can consider all uninfected cells (M_o, D_{mu}, R_{mu}) and infected cells (M_i, D_{mi}, R_{mi}). This approach reduces (26) to:

$$g_1(\hat{B}) = +\hat{a}_2 \hat{B}^2 + \hat{a}_1 \hat{B} + \hat{a}_0, \tag{27}$$

where

$$\begin{aligned}
\hat{a}_0 &= (s_0 + s_1)(\eta_1 + H_1\beta_1 + \eta_1 + H_1\beta_1\eta_2 + H_2\beta_2)(1 - \mathcal{R}_0), \\
\hat{a}_1 &= \delta\left(\frac{\phi_0 + \alpha_0 + \mu_0}{K} - (\beta_0 + \beta_1 + \beta_2)\right), \\
\hat{a}_1 &= \frac{\delta(\beta_0 + \beta_1 + \beta_2)}{K}.
\end{aligned} \tag{28}$$

The number of endemic equilibria depends on the signs and values of $\hat{a}_0$, $\hat{a}_1$, and $\hat{a}_2$. The bifurcation analysis summarized in Theorem 2.3 provides criteria for their existence.

Theorem 2.3: *The model* (18)–(24) *admits:*

(i) *a unique endemic equilibrium if* $\hat{a}_0 < 0$;
(ii) *a unique endemic equilibrium if* $\hat{a}_1 < 0$, *and* $\hat{a}_0 = 0$ *or* $\hat{a}_1 - 4\hat{a}_0\hat{a}_2 = 0$;
(iii) *two endemic equilibria if* $\hat{a}_1 < 0, \hat{a}_0 > 0$ *and* $\hat{a}_1 - 4\hat{a}_0\hat{a}_2 > 0$;
(iv) *no endemic equilibrium otherwise.*

To complete the analysis of the endemic equilibrium we will perform the the bifurcation analysis. We will make use of Center Manifold Theorem (CMT) as described in Castillo-Chavez et al. [39]. The CMT entails investigating the dynamical behaviors of model (18)–(24) in the neighbourhood of $\mathcal{E}^0$ and parameter values around $\mathcal{R}_0 = 1$ being governed by Equation (29):

$$u'(t) = au^2 + bu\beta_0 + \mathcal{O}(u^3), \tag{29}$$

where β_0 is the bifurcation parameter (with $\beta_0 = (\xi_1\beta_1, \xi_2\beta_2), \xi_1 > 0$ and $\xi_2 > 0$), β_0 is the center manifold of model (18)–(24) at $\mathcal{R}_0 = 1$. Moreover, corresponding expressions of a and b are determined in the next discussion. Thus, our focus is on determining the simple zero eigenvalue for $D_x f(x_0, \phi)|_{\mathcal{R}_0=1}$, and the corresponding

left and right eigenvectors v and w, such that $vw = 1$. Linearizing system (18)–(24) about the DFE leads to

$$G = \begin{bmatrix} -g_{11} & 0 & 0 & 0 & 0 & 0 & -\beta_0 M_0^* \\ 0 & -g_{22} & 0 & 0 & 0 & 0 & \beta_0 M_0^* \\ \phi_1 & 0 & -\mu_0 & 0 & 0 & 0 & -\beta_1 D_{mu}^* \\ 0 & \alpha_1 & 0 & -g_{44} & 0 & 0 & \beta_1 D_{mu}^* \\ 0 & 0 & 0 & 0 & -\mu_2 & 0 & -\beta_2 R_{mu}^* \\ 0 & 0 & 0 & 0 & 0 & -g_{66} & \beta_2 R_{mu}^* \\ 0 & g_{72} & 0 & g_{74} & 0 & g_{76} & -g_{77} \end{bmatrix}, \tag{30}$$

where

$$\begin{aligned} &g_{11} = (\phi_0 + \phi_1), \quad g_{22} = (\gamma^* + \alpha_0 + \alpha_1), \quad g_{44} = (\gamma^* + \mu_1), \quad g_{66} = (b + \gamma^*), \\ &g_{72} = (\gamma^* N_1 + N_0 \alpha_0), \quad g_{74} = (\gamma^* N_3 + N_2 \mu_1), \quad g_{76} = (N_4 b + \gamma^* N_5), \\ &g_{77} = \frac{\delta}{K} + M_0^* (H_0 \beta_0 + \eta_0) + D_{mu}^* (H_1 \beta_1 + \eta_1) + R_{mu}^* (H_2 \beta_2 + \eta_2) \end{aligned}$$

Making use of matrix G (30), the corresponding expression for w and v given by:

$$\begin{aligned} &w_1 = -\frac{M_o^* \beta_0 w_7}{g_{11}}, \quad w_2 = \frac{M_o^* \beta_0 w_7}{g_{22}}, \quad w_3 = -\frac{\left(D_{mu}^* g_{11} \beta_1 + M_o^* \beta_0 \phi_1\right) w_7}{g_{11} \mu_0}, \\ &w_4 = \frac{\left(M_o^* \alpha_1 \beta_0 + D_{mu}^* g_{22} \beta_1\right) w_7}{g_{22} g_{44}}, \quad w_5 = -\frac{R_{mu}^* \beta_2 w_7}{\mu_2}, \quad w_6 = \frac{R_{mu}^* \beta_2 w_7}{g_{66}}, \quad w_7 > 0, \end{aligned}$$

and;

$$v_1 = 0, \quad v_2 = \frac{v_7 (g_{44} g_{72} + g_{74} \alpha_1)}{g_{22} g_{44}}, \quad v_3 = 0, \quad v_4 = \frac{g_{74} v_7}{g_{44}}, \quad v_5 = 0, \quad v_6 = \frac{g_{76} v_7}{g_{66}}, \quad v_7 > 0.$$

Next, we determine the second-order partial derivatives of f for $\frac{\partial^2 f_i(x_0,\phi)}{\partial x_j \partial x_k}|_{\mathcal{R}_0=1}$ and $\frac{\partial^2 f_i(x_0,\phi)}{\partial x_j \partial \beta_0}|_{\mathcal{R}_0=1}$. One can easily verify that the non-zero elements second-order partial derivatives of f are:

$$\begin{aligned} &\frac{\partial^2 f_2(x_0,\phi)}{\partial x_1 \partial x_7} = 2\beta_0, \quad \frac{\partial^2 f_4(x_0,\phi)}{\partial x_3 \partial x_7} = 2\beta_1, \quad \frac{\partial^2 f_6(x_0,\phi)}{\partial x_5 \partial x_7} = 2\beta_2, \quad \frac{\partial^2 f_7(x_0,\phi)}{\partial x_1 \partial x_7} = -2(H_0\beta_0 + \eta_0), \\ &\frac{\partial^2 f_7(x_0,\phi)}{\partial x_3 \partial x_7} = -2(H_1\beta_1 + \eta_1), \quad \frac{\partial^2 f_7(x_0,\phi)}{\partial x_5 \partial x_7} = -2(H_2\beta_2 + \eta_2), \quad \frac{\partial^2 f_2(x_0,\phi)}{\partial \beta_0 \partial x_7} = M_o^*, \\ &\frac{\partial^2 f_4(x_0,\phi)}{\partial \beta_0 \partial x_7} = \xi_1 D_{mu}^*, \quad \frac{\partial^2 f_6(x_0,\phi)}{\partial \beta_0 \partial x_7} = \xi_2 R_{mu}^*. \end{aligned}$$

Based on formulae and results in Castillo-Chavez [39], we compute a and b as follows:

$$\begin{aligned} a &= \sum_{i,jk=1}^{7} v_i w_j w_k \frac{\partial^2 f_i(x_0,\phi)}{\partial x_j \partial x_k}|_{\mathcal{R}_0=1} \\ &= \frac{2M_o^* \beta_0}{g_{11}} \left((H_0\beta_0 + \eta_0) - \frac{\beta_0 (g_{44} g_{72} + g_{74} \alpha_1)}{g_{22} g_{44}} \right) w_7^2 v_7 + \frac{2R_{mu}^* \beta_2}{\mu_2} \left((H_2\beta_2 + \eta_2) - \frac{\beta_2 g_{76}}{g_{66}} \right) w_7^2 v_7 \\ &\quad + \frac{2\left(D_{mu}^* g_{11} \beta_1 + M_o^* \beta_0 \phi_1\right)}{g_{11} \mu_0} \left((H_1\beta_1 + \eta_1) - \frac{\beta_1 g_{74}}{g_{44}} \right) w_7^2 v_7, \end{aligned} \tag{31}$$

$$\begin{aligned} b &= \sum_{i,jk=1}^{7} v_i w_j \frac{\partial^2 f_i(x_0,\phi)}{\partial x_j \partial \theta}|_{\mathcal{R}_0=1} \\ &= M_o^* \left(\frac{(g_{44} g_{72} + g_{74} \alpha_1)}{g_{22} g_{44}} - H_0 \right) v_7 w_7 + D_{mu}^* \left(\frac{g_{74}}{g_{44}} - H_1 \right) v_7 w_7 + R_{mu}^* \left(\frac{g_{76}}{g_{66}} - H_2 \right) v_7 w_7 > 0. \end{aligned}$$

Based on the results in Equations (31), one can observe that $a > 0$ and $b > 0$, and this implies that model (1) admits a backward bifurcation at $\mathcal{R}_0 = 1$. The results are summarized in Theorem 2.4.

Theorem 2.4: *Model* (1)–(8) *admits a backward bifurcation at* $\mathcal{R}_0 = 1$.

2.6. Effects of optimized treatment regimen

Combination therapy for the treatment of Mtb, RIPE – is carefully designed to achieve multiple therapeutic aims. Primarily, these drug regimens are intended to deliver a strong early bactericidal effect, effectively reducing the population of actively dividing bacteria within the host in a relatively short period. Additionally, one of their key objectives is to sterilize infected tissues by eliminating residual bacterial reservoirs, thereby significantly lowering the risk of disease relapse after treatment completion. An equally important goal is to prevent the development of drug resistance, which can undermine the efficacy of therapy and pose significant challenges to disease management. To this end, these drugs are formulated to target both actively replicating and dormant, persistent bacterial forms – ensuring a comprehensive approach to infection eradication. The synergistic interaction among the drugs enhances their overall effectiveness: during the initial, intensive phase of treatment, they work collectively to rapidly decrease the bacterial load, while in the subsequent continuation phase, their focus shifts to eradicating persistent, non-replicating bacteria that are often resistant to individual drugs, thereby reducing the likelihood of relapse and increasing the chances of a complete cure [29–31].

To explore the potential benefits of optimized treatment strategies, we transform model (1)–(8) into an optimal control (OC) problem. Within this framework, we introduce two control functions, $u_1(t)$ and $u_2(t)$, which represent therapeutic activities that need to be maximized to effectively control Mtb infection. Specifically, the control $u_1(t)$ measures the drug combination's capacity to reduce the population of infected cells [32], while $u_2(t)$ reflects the ability of the therapy to inhibit Mtb replication and self-replication processes. The goal of this optimal control problem is to minimize the proliferation of Mtb, as well as the populations of infected macrophages, monocytes, and MDMs, through an appropriate choice of control functions. Mathematically, this can be represented by a payoff function that seeks to reduce bacterial replication and immune cell infection levels over the treatment period, thereby optimizing therapeutic outcomes and minimizing disease persistence:

$$J(u_1(t), u_2(t)) = \int_{t_0}^{t_f} \left(M_i(t) + D_{mi}(t) + R_{mi}(t) + B(t) + \frac{A_1 u_1^2(t)}{2} + \frac{A_2 u_2^2(t)}{2} \right) \mathrm{d}t, \tag{32}$$

subject to

$$\frac{\mathrm{d}M_o}{\mathrm{d}t} = s_0 - (\phi_0 + \phi_1)M_o - \beta_0 B M_o, \tag{33}$$

$$\frac{\mathrm{d}M_i}{\mathrm{d}t} = \beta_0 B M_o - (\alpha_0 + \alpha_1)M_i - \frac{\gamma M_i T}{a_0 + T} - u_1 M_i, \tag{34}$$

$$\frac{\mathrm{d}D_{mu}}{\mathrm{d}t} = \phi_1 M_o - \beta_1 B D_{mu} - \mu_0 D_{mu}, \tag{35}$$

$$\frac{\mathrm{d}D_{mi}}{\mathrm{d}t} = \alpha_1 M_i + \beta_1 B D_{mu} - \mu_1 D_{mi} - \frac{\gamma D_{mi} T}{a_1 + T} - u_1 D_{mi}, \tag{36}$$

$$\frac{\mathrm{d}R_{mu}}{\mathrm{d}t} = s_1 - \beta_2 B R_{mu} - \mu_2 R_{mu}, \tag{37}$$

$$\frac{\mathrm{d}R_{mi}}{\mathrm{d}t} = \beta_2 B R_{mu} - b R_{mi} - \frac{\gamma R_{mi} T}{a_2 + T} - u_1 R_{mi}, \tag{38}$$

$$\begin{aligned} \frac{\mathrm{d}B}{\mathrm{d}t} = {} & \delta B(1 - u_2)\left(1 - \frac{B}{K}\right) + (1 - u_1)\alpha_0 N_0 M_i + (1 - u_1)\frac{N_1 \gamma M_i T}{a_0 + T} + (1 - u_1) N_2 \mu_1 D_{mi} \\ & + (1 - u_1)\frac{N_3 \gamma D_{mi} T}{a_1 + T} + (1 - u_1) N_4 b R_{mi} + (1 - u_1)\frac{N_5 \gamma R_{mi} T}{a_2 + T} + u_1(M_i + D_{mi} + R_{mi}) \\ & - (\eta_0 + H_0\beta_0) B M_o - (\eta_1 + H_1\beta_1) B D_{mu} - (\eta_2 + H_2\beta_2) B R_{mu}, \end{aligned} \tag{39}$$

$$\frac{\mathrm{d}T}{\mathrm{d}t} = s_3 + \frac{c_0 M_i T}{1 + e_0 T} + \frac{c_1 D_{mi} T}{1 + e_1 T} + \frac{c_2 R_{mi} T}{1 + e_2 T} + \frac{c_3 B T}{1 + e_3 T} - \sigma T. \tag{40}$$

The OC problem is considered to start at time zero t_0 and to run for a fixed duration t_f. In defining the payoff function, the positive constants A_1 and A_2 represent the weights associated with the control variables $u_1(t)$ and $u_2(t)$, respectively. It is also important to note that quadratic payoff functions have been employed. The choice

of mathematical functions to model drug efficacy and dose-response relationships is a well-documented and debated topic in pharmacodynamics and biostatistics. Some studies utilize piece-wise linear payoff functions [40, 41], while others adopt linear payoff functions [42–45].

Quadratic payoff functions are also commonly used [46–48]. Overall, quadratic payoff functions are favored due to their desirable mathematical properties, such as their smoothness and the presence of only a single extremum, which facilitates the determination of optimal solutions [49]. From a biological perspective, quadratic terms impose a harsher penalty on large control values compared to small ones. This feature is particularly relevant in treatments like chemotherapy, where excessive control measures can be detrimental. Consequently, quadratic payoff functions are often preferred in such contexts [49].

Consequently, the optimal control problem involves finding control functions that optimize the specified payoff, leading to the determination of optimal strategies within this framework. $U = (u_1^*(t), u_2^*(t))$, such that

$$J(u_1^*(t), u_2^*(t)) = \inf_{(u_1,u_2)\in U} J(u_1(t), u_2(t)),$$

for the admissible set $U = \{(u_1(t), u_2(t)) \in (L^\infty(0, t_f))^2 : 0 \le u_i(t) \le u_{i\max}; u_{i\max} \in \mathbb{R}^+, i = 1, 2\}$, where $u_{i\max}$ denotes the upper bound of the controls. The optimal control problem (33)–(40) can be reduced to minimizing the corresponding Hamiltonian with respect to u_1 and u_2

$$\mathcal{H}(t, \mathbf{x}, \mathbf{u}, \lambda) = M_i(t) + D_{mi}(t) + R_{mi}(t) + B(t) + \frac{A_1 u_1^2(t)}{2} + \frac{A_2 u_2^2(t)}{2} + \lambda_k f_k \tag{41}$$

where $\lambda = [\lambda_1(t), \lambda_2(t), \ldots, \lambda_7(t)]$ are the adjoint variable for a 7 dimensional state, that is., $\mathbf{x} = (M_o, M_i, D_{mu}, D_{mi}, R_{mu}, R_{mi}, B, T)$, $\mathbf{u} = (u_1, u_2)$, and f_k is the right hand side of model (33)–(40) with $k = 1, 2, \ldots, 7$. The Hamiltoniam is constructed to satisfy the first the following relation $\frac{\partial \mathcal{H}}{\partial \mathbf{x}} = -\frac{\mathrm{d}\lambda}{\mathrm{d}t}$, that is:

$$\begin{aligned}
\frac{\mathrm{d}\lambda_1}{\mathrm{d}t} &= \lambda_1(\phi_0 + \phi_1) + \beta_0 B(\lambda_1 - \lambda_2) - \lambda_7(\eta_0 + H_0\beta_0)B,\\
\frac{\mathrm{d}\lambda_2}{\mathrm{d}t} &= -1 + \lambda_2\left((\alpha_0 + \alpha_1 + u) + \frac{\gamma T}{a_0 + T} + u_1\right) - \lambda_4\alpha_1 - \lambda_7(1 - u_1)\left(1 + \alpha_0 N_0 + \frac{N_1\gamma T}{a_0 + T}\right)\\
&\quad - \lambda_8\frac{c_0 T}{1 + e_0 T},\\
\frac{\mathrm{d}\lambda_3}{\mathrm{d}t} &= \lambda_3(\beta_1 B + \mu_0) - \lambda_4\beta_1 B,\\
\frac{\mathrm{d}\lambda_4}{\mathrm{d}t} &= -1 + \lambda_4\left(u_1 + \mu_1 + \frac{\gamma T}{a_1 + T}\right) - \lambda_7(1 - u_1)\left(1 + N_2\mu_1 + \frac{N_3\gamma T}{a_1 + T}\right) - \lambda_8\frac{c_1 T}{1 + e_1 T},\\
\frac{\mathrm{d}\lambda_5}{\mathrm{d}t} &= \lambda_5(\beta_2 B + \mu_2) - \lambda_6\beta_2 B + \lambda_7(\eta_2 + H_2\beta_2)B_2,\\
\frac{\mathrm{d}\lambda_6}{\mathrm{d}t} &= -1 + \lambda_6\left(b + u_1 + \frac{\gamma T}{a_2 + T}\right) - \lambda_7(1 - u_1)\left(1 + N_4 b + \frac{N_5\gamma T}{a_2 + T}\right) - \lambda_8\frac{c_2 T}{1 + e_2 T},\\
\frac{\mathrm{d}\lambda_7}{\mathrm{d}t} &= -1 + \lambda_1\beta_0 M_o(\lambda_1 - \lambda_2) + \beta_1 D_{mu}(\lambda_3 - \lambda_4) + \beta_2 R_{mu}(\lambda_5 - \lambda_6) + \lambda_7\frac{\delta(1 - u_2)}{K}\\
&\quad + \lambda_7(\eta_0 + H_0\beta_0)M_o + \lambda_7(\eta_1 + H_1\beta_1)D_{mu} + \lambda_7(\eta_2 + H_2\beta_2)R_{mu} - \lambda_8\frac{c_3 T}{1 + e_3 T},\\
\frac{\mathrm{d}\lambda_8}{\mathrm{d}t} &= \lambda_2\gamma M_i\left(\frac{1}{a_0 + T} - \frac{T}{(a_0 + T)^2}\right) + \lambda_4\gamma D_{mi}\left(\frac{1}{a_1 + T} - \frac{T}{(a_1 + T)^2}\right) + \lambda_6\gamma R_{mi}\left(\frac{1}{a_2 + T} - \frac{T}{(a_2 + T)^2}\right)\\
&\quad - \lambda_7(1 - u_1)N_1\gamma M_i\left(\frac{1}{a_0 + T} - \frac{T}{(a_0 + T)^2}\right) - \lambda_7(1 - u_1)N_3\gamma D_{mi}\left(\frac{1}{a_1 + T} - \frac{T}{(a_1 + T)^2}\right)\\
&\quad - \lambda_7(1 - u_1)N_5\gamma R_{mi}\left(\frac{1}{a_2 + T} - \frac{T}{(a_2 + T)^2}\right) - \sigma\lambda_8 + \lambda_8\left(\frac{1}{1 + e_0 T} - \frac{e_0(c_0 M_i + T)}{(1 + e_0 T)^2}\right)\\
&\quad + \lambda_8\left(\frac{1}{1 + e_1 T} - \frac{e_1(c_1 D_{mi} + T)}{(1 + e_1 T)^2}\right) + \lambda_8\left(\frac{1}{1 + e_2 T} - \frac{e_2(c_2 R_{mi} + T)}{(1 + e_2 T)^2}\right)
\end{aligned}$$

Table 2. Forward-backward sweep iterative method.

Algorithm
1. Subdivide the time interval $[t_0, t_f]$ into N equal subintervals. Set the state variable at different times as $x = x(t)$ and assume a piecewise-constant control $u_j^{(0)}(t), t \in [t_k, t_{k+1}]$, where $k = 0, 1, 2, \ldots, N-1$ and $j = 1, 2$.
2. Apply the assumed control $u_j^{(0)}(t)$ to integrate the state system with an initial condition $x(t_0) = \mathbf{x}(0)$,forward in time $[t_0, t_f]$ using the fourth-order Runge-Kutta method, where $\mathbf{x}_0 = (M_0(0), M_i(0), D_{mu}(0), D_{mi}(0), R_{mu}(0), R_{mi}(0), B(0), T(0))$.
3. Apply the assumed control $u_j^{(0)}(t)$ to integrate the costate system with the transversality condition $\vec{\lambda}(t_f) = \lambda_i(t_f)$, $i = 1, 2, 3, \ldots,$ backward in time $[t_0, t_f]$ using the fourth-order Runge-Kutta method.
4. Update the control by entering the new state and costate solutions $\vec{x}(t)$ and $\vec{\lambda}(t_f)$, respectively, through the characterization equation (43).
5. STOP the algorithm if $\frac{\|\vec{x}^{i+1} - \vec{x}^{i}\|}{\|\vec{x}^{i+1}\|} < \xi$; otherwise update the control using a convex combination of the current and previous control and GO to step 2. Here, $\vec{x}^{i}$ is the ith iterative solution of the state system and ξ is an arbitrarily small positive quantity (Tolerance level). We set $\xi = 10^{-6}$ and use a step size of 10^{-4}.

$$+ \lambda_8 \left(\frac{1}{1 + e_3 T} - \frac{e_3 (c_3 B + T)}{(1 + e_3 T)^2} \right). \tag{42}$$

Furthermore, the optimality condition is determined by minimizing the Hamiltonian $\frac{\partial \mathcal{H}}{\partial \mathbf{u}} = 0$. Thus, the optimal controls are characterized by:

$$u_1^* = \min \left\{ u_{1\max}, \max \left\{ 0, \frac{\mathcal{A}}{A_1} \right\} \right\}, \quad u_2^* = \min \left\{ u_{2\max}, \max \left\{ 0, \frac{\delta (K - B) \lambda_7}{K A_2} \right\} \right\}, \tag{43}$$

where:

$$\mathcal{A} = M_i \left(\lambda_2 - \lambda_7 N_0 \alpha_0 - \lambda_7 \frac{N_1 \gamma T}{a_0 + T} \right) + D_{mi} \left(\lambda_4 - \lambda_7 N_2 \mu_1 - \lambda_7 \frac{N_3 \gamma T}{a_1 + T} \right) + R_{mi} \left(\lambda_6 - \lambda_7 N_4 b - \lambda_7 \frac{N_5 \gamma T}{a_2 + T} \right).$$

In (43), $u_{1\,\max} \leq 1$ and $u_{2\,\max} \leq 1$ are the feasible upper bounds of the controls $u_1(t)$ and $u_2(t)$, respectively.

3. Numerical results and discussions

To support the analytical findings presented in this study, this section conducts comprehensive numerical simulations of the models described by systems (1)–(8) and (33)–(40). The simulations were performed using MATLAB R2024a. To numerically solve the proposed optimal control problem (system (33)–(40)), solutions were obtained by solving the associated optimality system comprising eight ordinary differential equations derived from the state and costate equations. The method employed is commonly known as the forward-backward sweep iterative technique [50]. The procedure begins with an initial guess for the control variables over the simulated time horizon. The state equations are then integrated forward in time using the fourth-order Runge-Kutta scheme. Subsequently, the control variables are updated via a convex combination of their previous values and the values obtained from the optimality conditions. This iterative process is repeated until the solutions converge, i.e. until the difference between successive iterations falls below a predefined tolerance level [50]. Table 2 summarizes the essential steps of the forward-backward sweep method. For a more detailed discussion, the reader is referred to [50].

These simulations are designed to validate and illustrate the theoretical results derived earlier. We utilize specific parameter values listed in Table 3, which have been carefully selected and adapted from reputable, peer-reviewed journal articles to ensure the accuracy and relevance of our simulations.

3.1. Sensitivity analysis of the reproduction number

In this subsection, we investigate the impact of model parameters on the transmission potential of *Mtb* within the host. Specifically, we study the sensitivity analysis of the reproduction number. We use the Latin hypercube sampling technique and the partial rank correlation coefficients (PRCC) method in Marino et al. [51]. The sign

Table 3. Model parameters and their interpretations.

Symbol	Biological definition	Baseline value	Source
s_0	Recruitment rate of circulating monocytes into lung tissue	$5 \times 10^9(10^4 - 10^{10})$ cells ml^{-1}day^{-1}	[52]
ϕ_0	Natural death rate of uninfected monocytes	$0.33(0.33-1)$ day^{-1}	[28]
ϕ_1	Differentiation rate of monocytes to MDMs	$0.1(0.1-0.5)$ day^{-1}	[28]
b	Infected macrophages clearance rate	$0.11(0.05, 0.5)$day^{-1}	[16]
β_0	Infection rate of monocytes by Mtb$B$	$10^{-8}(10^{-8} - 10^{-5})$ ml/cell $\cdot$ day	[16]
β_1	Infection rate of MDMs by Mtb	$10^{-8}(10^{-8} - 10^{-5})$ ml/cell $\cdot$ day	[16]
β_2	Infection rate of RAM by Mtb	$10^{-8}(10^{-8} - 10^{-5})$ ml/cell $\cdot$ day	[16]
α_0	Natural death rate of infected monocytes	$0.2(0.2-0.5)$ day^{-1}	[28]
α_1	Conversion rate of infected monocytes to infected MDMs	$0.05(0.05-0.2)$ day^{-1}	[28]
γ	Max rate of T-cell mediated lysis	$1.5(0.1-2)$ day^{-1}	[16]
a_0, a_1, a_2	Saturation constants for T-cell lysis	$3(0.3, 30)$	[16]
s_1	Recruitment rate of resident macrophages	$5000(3300, 7000)$ ml^{-1}day^{-1}	[16]
μ_0	Natural death rate of susceptible MDMs	$0.1-0.3$ day^{-1}	[28]
μ_1	Natural death rate of infected MDMs	$0.2(0.2-0.5)$ day^{-1}	[28]
μ_2	Natural death rate of RAMs	$0.01(0.01-0.2)$ day^{-1}	[16]
δ	Bacterial logistic growth rate	$5 \cdot 10^{-4}(0, 0.26)$ day^{-1}	[16]
K	Carrying capacity for bacteria	$10^6(10^6, 10^{10})$ ml^{-1}	[16]
$N_0, N_1, N_2, N_3, N_4, N_5$	Mean population of Mtb released by one macrophage	$50(50, 100)$	[16]
η_0, η_1, η_2	Bacterial clearance rates by immune cells	$10^{-7} - 10^{-6}$ ml/cell $\cdot$ day	[16]
H_0, H_1, H_2	Mean number of Mtb carried by one macrophage	$25(25, 50)$	[16]
c_0, c_1, c_2, c_3	T-cell activation rates via infected cells	$10^{-2}(0.01, 0.1)$	[16]
e_0, e_1, e_2, e_3	Saturation constants for T-cell activation	$10(10^{-6}, 10^2)$ cells	[16]
s_3	Baseline T-cell production rate	$6.6(0.33, 33)$ ml^{-1}day^{-1}	[16]
σ	T-cell decay rate	$0.33(0.05, 0.33)$ day^{-1}	[16]

of the PRCC value demonstrates whether the parameter is inversely or positively correlated to the output. A model parameter with an absolute PRCC value close to unity has a significance influence on the output [51].

Simulation results, illustrated in Figure 2 and supported by the numerical data presented in Table 4, elucidate the relationships between various model parameters and the basic reproduction number $\mathcal{R}_0$. These relationships are derived from Partial Rank Correlation Coefficients (PRCC) and their corresponding p-values. Parameters with p-values less than 0.05 are considered to have a statistically significant association with $\mathcal{R}_0$, suggesting that variations in these parameters are likely to influence the transmission potential of the infection as represented by $\mathcal{R}_0$. Notably, certain parameters such as the monocyte recruitment rate (s_0), the infection rates of different macrophage populations ($\beta_0, \beta_1, \beta_2$), and the differentiation rates of monocytes into macrophages (ϕ_0, ϕ_1) exhibit positive correlations with $\mathcal{R}_0$. This indicates that increases in these parameters tend to elevate $\mathcal{R}_0$, thereby potentially enhancing the infectiousness and spread of the pathogen within the host environment. Conversely, parameters such as the natural death rate of resident alveolar macrophages (μ_2), and the maximum rate of T-cell mediated lysis (γ), show strong negative correlations. These findings imply that higher values of these parameters are associated with reductions in $\mathcal{R}_0$, possibly curbing the infection's transmission. The magnitude and sign of the PRCCs, coupled with the very low p-values, underscore the pivotal role of these parameters as key determinants of the infection's transmission dynamics. Parameters exhibiting non-significant p-values are less likely to exert a substantial impact on $\mathcal{R}_0$ and may be deprioritized when designing intervention strategies. Overall, this analysis emphasizes the importance of targeting specific parameters – particularly those with significant correlations – for effective control and management of Mtb infection.

To further assess the relationship between $\mathcal{R}_0$ and each individual's parameter identified in Figure 2 as having a significant relationship with $\mathcal{R}_0$, we carried out a Monte Carlo simulation of 2,000 sample values for each parameter. The output is illustrated in Figure 3. Within each plot, a colored dot represents one parameter combination, and the red dotted line illustrates the trend in the relationship between $\mathcal{R}_0$ and the focal parameter, averaged over all parameter combinations. Overall, we observe that the trend line for model parameters that are positively correlated with $\mathcal{R}_0$ has a positive gradient, and the reverse is true for parameters negatively correlated with $\mathcal{R}_0$. The steepness of the trend line increases as the strength of the relationship between $\mathcal{R}_0$ and the parameter increases.

Sensitivity analysis demonstrated that the infection rate of the Mtb pathogen on immune cells – specifically monocytes and macrophages – exerts a significant influence on the within-host dynamics. To further investigate this relationship, we conducted simulations of the model (1)–(8), varying the parameters β_i for $i = 0,1,2$.

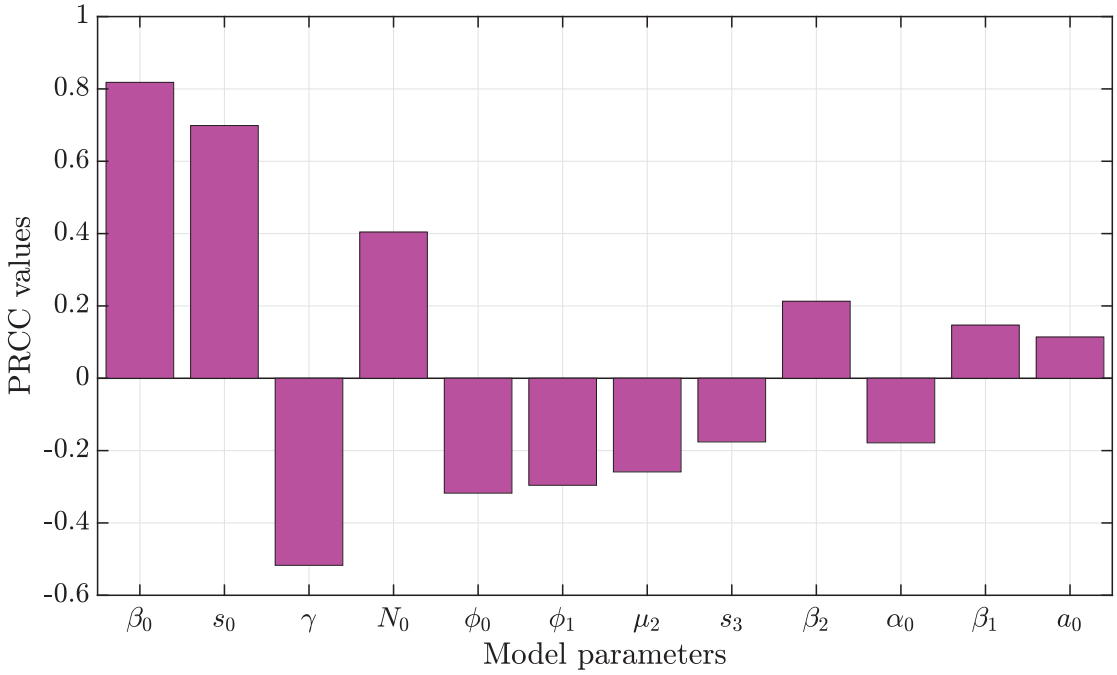

Figure 2. Sensitivity analysis of $\mathcal{R}_0$, illustrating how variations in model parameters influence its estimated value and the potential implications for disease transmission dynamics. Note that only the most sensitive parameters are included in this graphical presentation; the effects of all parameters on $\mathcal{R}_0$ are detailed in Table 4.

Table 4. Model parameters and their *p*-values.

Parameter	PRCC	*P*-value	Parameter	PRCC	*P*-value	Parameter	PRCC	*P*-value
s_0	0.6987	0.0000	ϕ_0	−0.3176	0.0000	ϕ_1	0.2959	0.0000
β_0	0.8182	0.0000	β_1	0.1093	0.0000	β_2	0.2365	0.0000
α_0	−0.1659	0.0000	α_1	−0.1044	0.0000	γ	−0.5172	0.0000
a_0	0.1083	0.0000	a_1	0.0098	0.6626	a_2	−0.0020	0.9303
s_1	0.0830	0.0002	μ_0	0.0356	0.1115	μ_1	0.0208	0.3522
μ_2	−0.2589	0.0000	δ	0.0052	0.8167	N_0	0.4043	0.0000
N_1	0.0443	0.0477	N_2	0.0290	0.1944	N_3	0.0575	0.0102
N_4	0.0474	0.0340	N_5	0.0611	0.0062	η_0	0.0259	0.2475
η_1	−0.0176	0.4310	η_2	0.0247	0.2703	H_0	−0.0282	0.2077
H_1	−0.0414	0.0642	H_2	−0.0473	0.0346	s_3	−0.1814	0.0000
b	−0.0044	0.8452	σ	−0.1760	0.0000			

The simulation results are presented in Figure 4. From these results, it is evident that an increase in the infection rate leads to a substantial rise in the populations of infected monocytes, macrophages, and the Mtb bacteria itself. Additionally, as the infection rate β_i increases, these populations grow rapidly and tend to attain their respective endemic equilibrium states within a period of less than 100 days.

Within the context of within-host dynamics, it is well-established that the pathogenicity of Mtb is typically higher in individuals with compromised immune systems. Therefore, these findings highlight the significant impact of tuberculosis progression in individuals with varying immune strengths. Specifically, the results illustrate how a stronger immune response can mitigate infection proliferation, whereas a weaker immune response facilitates rapid bacterial growth and immune cell infection.

Figure 5 demonstrates the occurrence of a backward bifurcation, supporting Theorem 2.4. This bifurcation, generated using $g_1(\hat{B})$ from Equation (27) with parameters listed in Table 3, indicates that the model admits multiple equilibrium points under certain conditions. Importantly, it suggests that simply reducing the basic reproduction number $\mathcal{R}_0$ below 1 does not guarantee disease eradication, as a stable endemic equilibrium can still exist. Therefore, control strategies solely focused on lowering $\mathcal{R}_0$ below 1 may be ineffective, emphasizing the need to consider the system's bifurcation structure

The simulation results presented in Figure 6 illustrate the impact of varying the parameter η_i, which represents the strength of the immune system in clearing Mtb bacteria. The results indicate that higher values of η_i

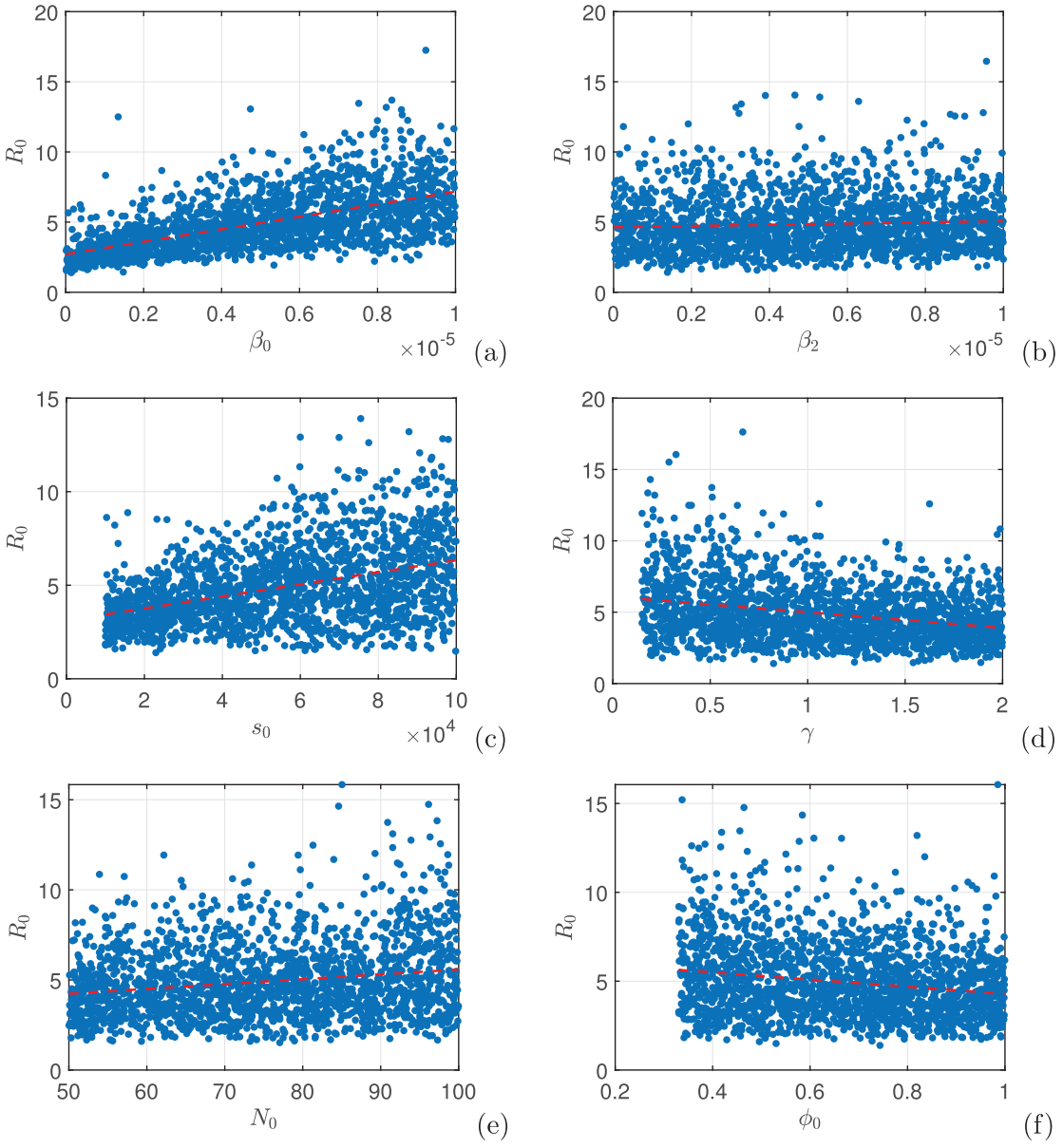

Figure 3. Monte Carlo simulations involving 1000 sample values for six illustrative parameters, which were selected using Latin Hypercube Sampling to efficiently explore parameter space and capture variability in the model outcomes.

significantly decrease the Mtb bacterial load, thereby reducing the overall bacterial population within the host. Consequently, this also leads to a reduction in the number of infected immune cells. Furthermore, these findings are consistent with earlier observations depicted in Figure 4, which demonstrate that the pathogenicity of Mtb tends to be higher in individuals with compromised immune responses. Specifically, a diminished immune clearance capacity, represented by lower η_i values, correlates with increased bacterial proliferation and greater immune cell infection, emphasizing the critical role of immune efficacy in controlling Mtb infection.

Simulation results, as depicted in Figure 7, illustrate the impact of an optimized treatment regimen on the within-host dynamics of Mtb over time, particularly under conditions of a low upper bound on the control variables. The results demonstrate that implementing the optimized treatment significantly reduces the populations of infected cells and the bacterial load of Mtb. These reductions are associated with a modest increase in the population of uninfected derived macrophages and a substantial increase in the resident macrophage population. Notably, these changes become observable shortly after the initiation of treatment, approximately 50 days into the regimen.

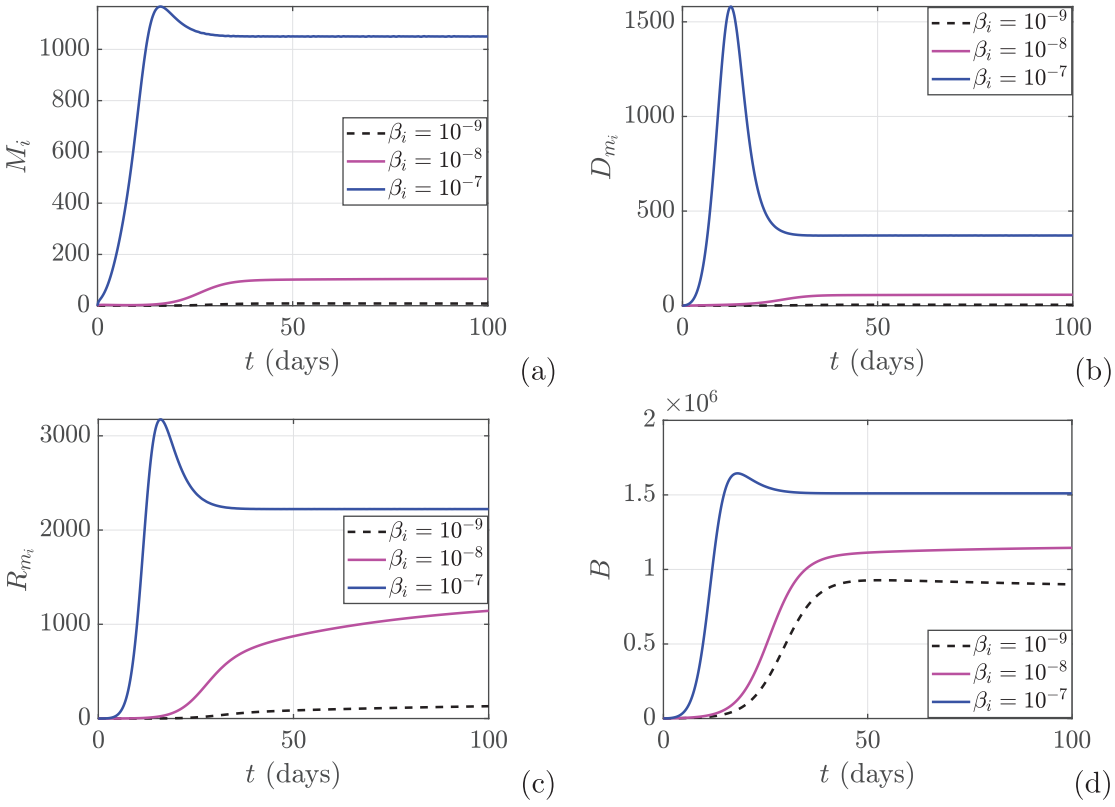

Figure 4. Simulation results illustrating the impact of varying Mtb infection rates on immune cell populations and infection outcomes. The initial conditions are: $M_o(0) = 10^6, M_i(0) = 0, D_{mu}(0) = 0, D_{mi}(0) = 0, R_{mu}(0) = 5000, B(0) = 10^3$, and $T(0) = 50$. Other model parameters are as listed in Table 3. Panel (a) shows infected monocytes M_i; (b) displays infected MDMs D_{mi}; (c) depicts infected resident macrophages R_{mi}; and (d) illustrates the Mtb population B.

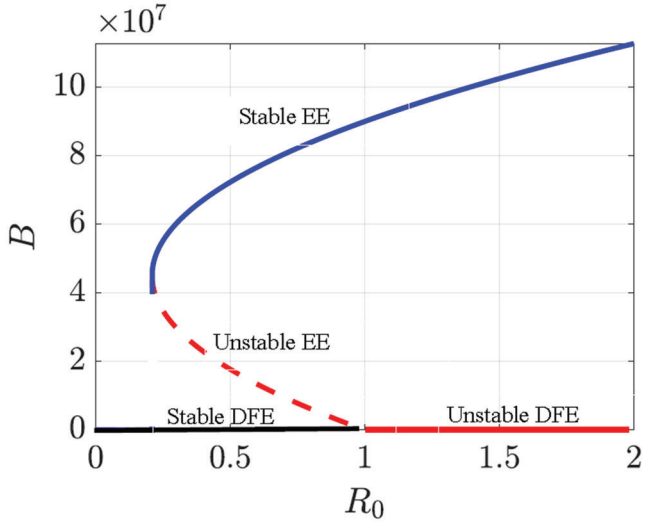

Figure 5. Bifurcation diagram of model (1)–(8) illustrating the occurrence of a backward bifurcation at the basic reproduction number $\mathcal{R}_0$. The graphical illustration was generated using $g_1(\hat{B})$ Equation (27). The solid black line indicates the interval where a stable disease-free equilibrium (DFE) exists. The solid red line represents the region where the DFE becomes unstable. The dotted red line shows the region where the endemic equilibrium (EE) is unstable, while the continuous blue line depicts the region where the EE is stable. These regions highlight the coexistence of multiple equilibria and the complex bifurcation behavior of the model. All other parameter values used in the analysis are consistent with those specified in Table 3.

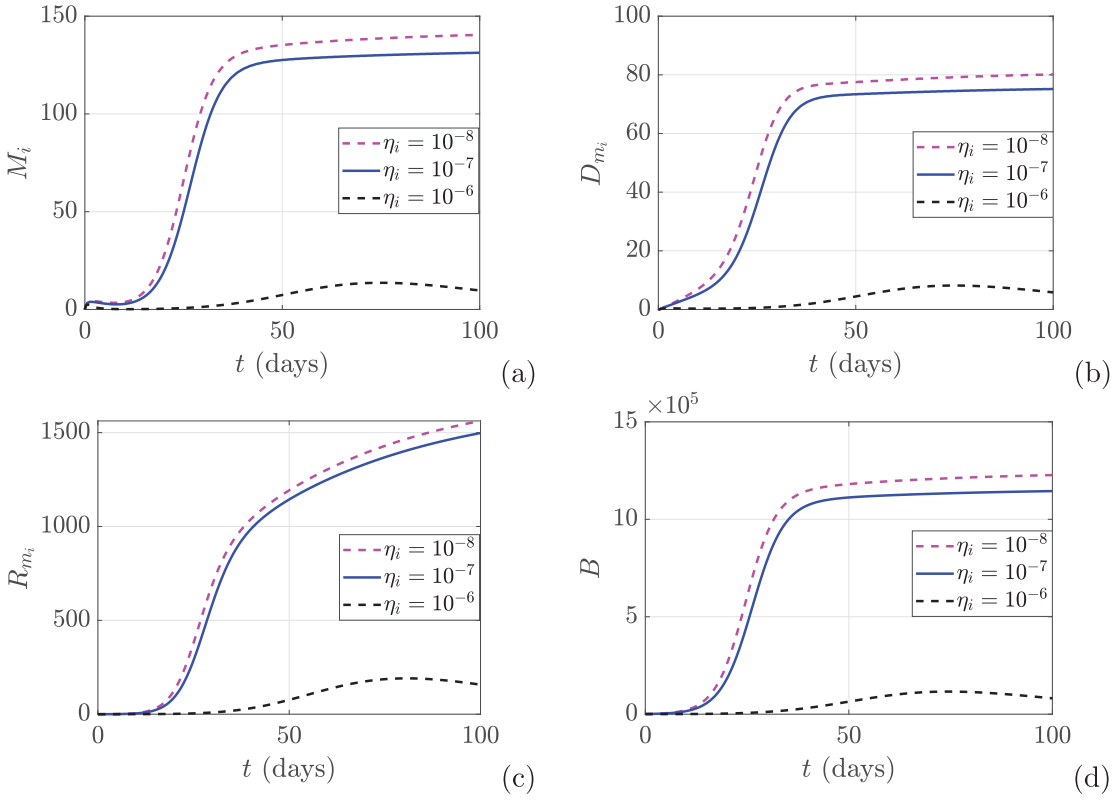

Figure 6. Simulation results demonstrating the influence of varying η_i (for $i = 0,1,2$) on within-host pathogen dynamics over time. The initial conditions for the model variables are specified as follows: $M_o(0) = 10^6$, $M_i(0) = 0$, $D_{mu}(0) = 0$, $D_{mi}(0) = 0$, $R_{mu}(0) = 5000$, $B(0) = 10^3$, and $T(0) = 50$. All other model parameters are adopted from the values listed in Table 3. Panel (a) shows infected monocytes M_i; (b) displays infected MDMs D_{mi}; (c) depicts infected resident macrophages R_{mi}; and (d) illustrates the Mtb population B.

In contrast, the population of monocytes appears to be unaffected by the treatment, exhibiting minimal or no significant variation over time. Importantly, the simulation outcomes suggest that these treatment strategies do not lead to the complete eradication of Mtb bacteria or infected cells. Instead, they maintain these populations at persistently low levels throughout the duration of the treatment period.

Furthermore, the control profiles, as observed in the simulations, initially commence at a low value of approximately 0.2. This initial value is attributable to the initial conditions, where the infected cell populations are set to zero. Subsequently, the control variables increase sharply to their respective maximum values and remain at these levels for the entire treatment duration. Overall, these findings imply that, while the optimized treatment regimen effectively suppresses pathogen populations and influences immune cell dynamics, it does not achieve complete clearance of the infection. Instead, it sustains the infection at a controlled, low-level state, which may help reduce disease progression and transmission risk over time.

Figure 8 illustrates the optimal control strategies when higher upper bounds are imposed on the control variables, specifically $0 \leq u_1 \leq 0.85$ and $0 \leq u_2(t) \leq 0.9$. As observed in previous analyses, the optimized treatment regimen significantly reduces the within-host Mtb population. In this scenario, the increased upper bounds on the control variables facilitate more aggressive treatment strategies, which lead to a rapid decline in both the infected cell population and the Mtb load. Notably, under these conditions, the infected cell and bacterial populations can be effectively eliminated within approximately 20 days of initiating the treatment regimen. This rapid eradication underscores the potential effectiveness of intensified treatment protocols when higher control limits are feasible. Overall, these findings suggest that maximizing control efforts within permissible bounds can substantially improve treatment outcomes, leading to quicker clearance of infection.

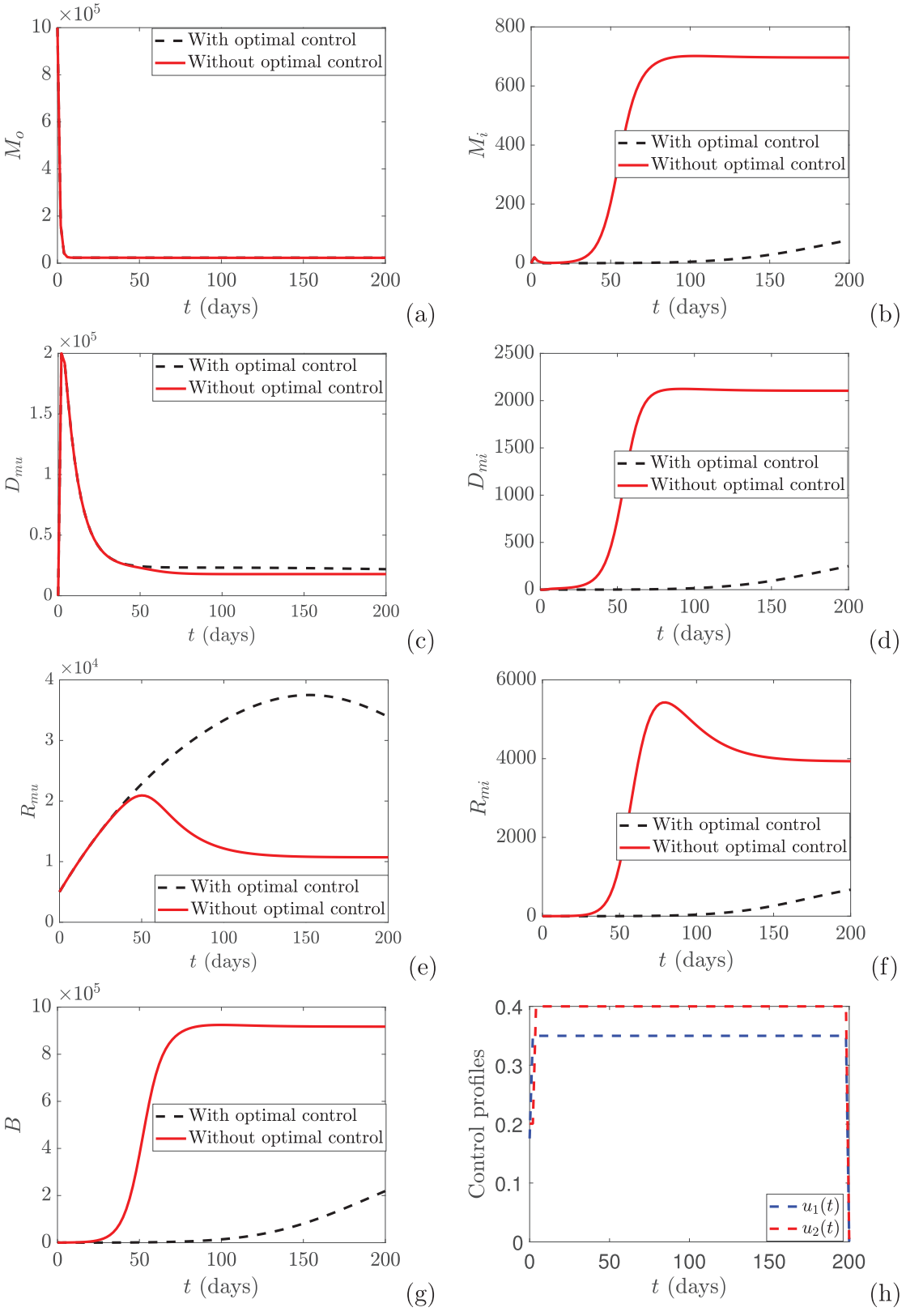

Figure 7. Simulation results showing the effect of an optimized treatment regimen on within-host pathogen dynamics. Initial conditions are $M_o(0) = 10^6, M_i(0) = 0, D_{mu}(0) = 0, D_{mi}(0) = 0, R_{mu}(0) = 5000, B(0) = 10^3, T(0) = 50$. Control constraints are $0 \leq u_1 \leq 0.35, 0 \leq u_2 \leq 0.4$, with weights $A_1 = A_2 = 10^{-8}$, based on parameters in Table 3. Panels show: (a) uninfected monocytes, (b) infected monocytes, (c) uninfected MDMs, (d) infected MDMs, (e) uninfected resident macrophages, (f) infected resident macrophages, (g) Mtb population, and (h) control profiles.

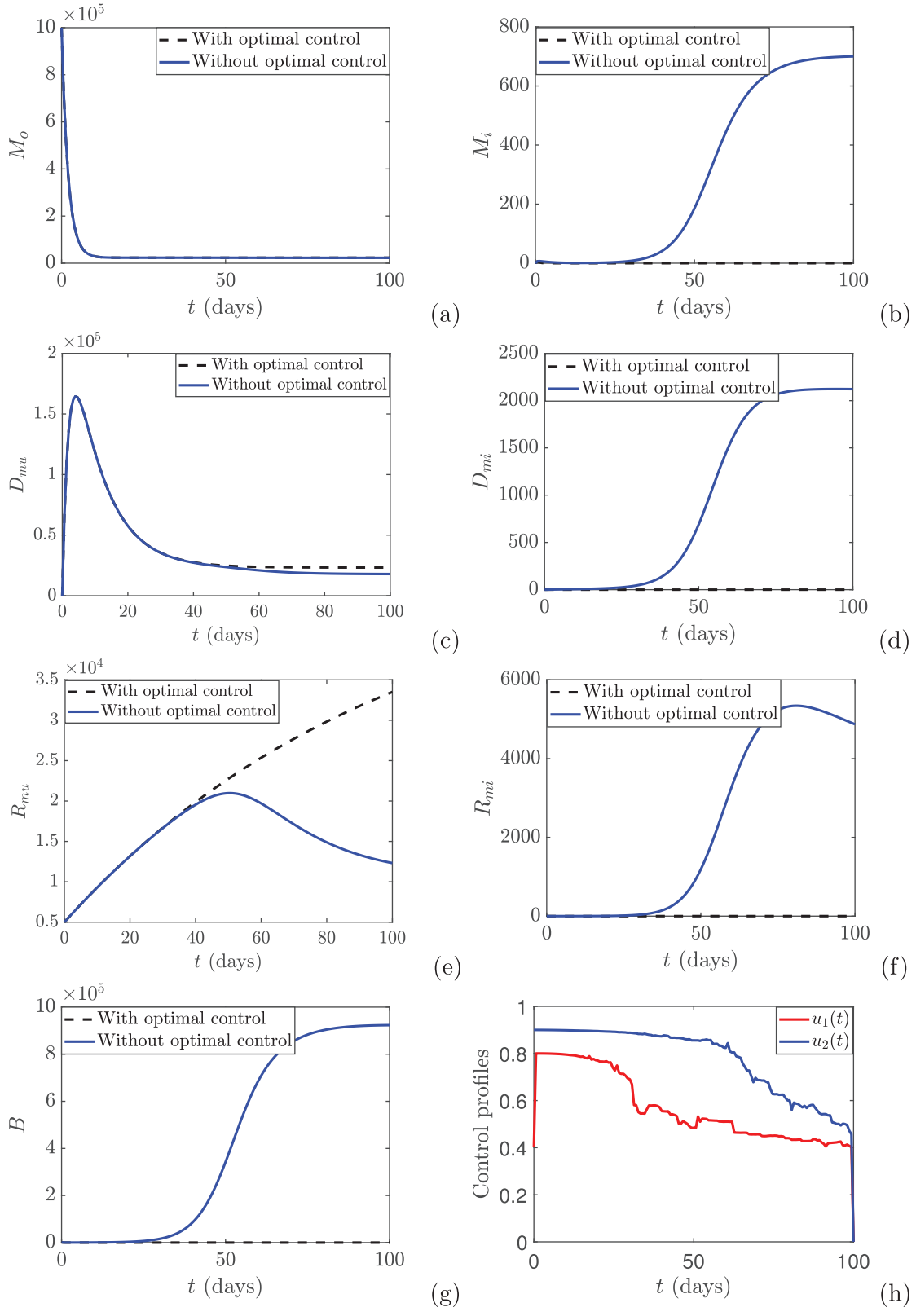

Figure 8. Simulation results illustrating the impact of an optimized treatment regimen on within-host pathogen dynamics over time. The initial conditions for the model variables are specified as follows: $M_o(0) = 10^6$, $M_i(0) = 0$, $D_{mu}(0) = 0$, $D_{mi}(0) = 0$, $R_{mu}(0) = 5000$, $B(0) = 10^3$, and $T(0) = 50$. The treatment control variables are constrained within the ranges $0 \leq u_1 \leq 0.85$ and $0 \leq u_2 \leq 0.9$, with weights set as $A_1 = A_2 = 10^{-8}$. All other model parameters are adopted from the values listed in Table 3. The panels depict: (a) uninfected monocytes, (b) infected monocytes, (c) uninfected MDMs, (d) infected MDMs, (e) uninfected resident macrophages, (f) infected resident macrophages, (g) Mtb population, and (h) control profiles.

Table 5. Comparison of representative within-host tuberculosis models.

Study	Model Type	Key Biological Components	Main Objective	Key Findings	Limitations
Wigginton and Kirschner [6]	ODE	Macrophages, $CD4^+$ T cells, Mtb	Immune regulation of TB	Macrophage–T-cell interactions are critical	No treatment dynamics
Marino and Kirschner [7]	ODE	Macrophages, T cells, cytokines, Mtb	Granuloma formation	Cytokine regulation is essential	No treatment component
Segovia-Juarez et al. [10]	ABM	Immune cells, Mtb, granuloma	Granuloma development	Identified key granuloma drivers	Simplified immunity and pathology
Day et al. [13]	ODE	Macrophages, intracellular bacteria	Chemotherapy effects	Treatment timing affects clearance	Simplified immune response
Ray et al. [14]	PDE	Spatial bacteria, immune cells	TNF-mediated control	TNF functions act synergistically	No treatment or lymph-node dynamics
Pienaar & Lerm [15]	ODE	Macrophages, intracellular/extracellular Mtb	Early infection dynamics	Macrophage activation determines outcome	No adaptive immunity or treatment
Joslyn et al. [20]	Hybrid	Granulomas, macrophages, T cells, cytokines	Predict TB outcomes	Early immunity predicts disease outcome	Limited to pulmonary TB
Helikumi et al. [22]	ODE + OC	Drug-sensitive/resistant Mtb, macrophages	Optimize TB therapy	Backward bifurcation; high efficacy controls infection	No spatial dynamics
Present study	ODE + OC	Monocytes, macrophages, T cells, Mtb	TB persistence and control	Backward bifurcation; immune response drives outcomes	No spatial or stochastic effects

4. Comparison with other studies

We developed a within-host mechanistic model for Mycobacterium tuberculosis (Mtb) to understand the pivotal role of monocytes in the immune response and to evaluate the implications of optimizing treatment regimens. Prior to our work, several mechanistic models of Mtb exist in the literature [6–24]. These models have significantly advanced our understanding of Mtb dynamics. In these prior studies, various techniques have been employed to formulate the models, including NODEs, agent-based models (ABMs), partial differential equations (PDEs), and fractional-order differential equations (FODEs). The main biological components incorporated into these models vary depending on the specific research questions. In this section, we will provide an overview of previous models, compare their approaches and findings with our work, and summarize these in Table 5.

5. Discussion and conclusions

This study provides a comprehensive mathematical framework for understanding the within-host dynamics of Mtb infection, emphasizing the pivotal role of monocytes in the immune response. The model integrates key cellular populations, including uninfected and infected monocytes, macrophages, resident macrophages, and T lymphocytes, along with the bacterial load. Rigorous analysis derived the basic reproduction number $\mathcal{R}_0$, serving as a threshold parameter indicating whether the infection persists or dies out within the host. Bifurcation analysis revealed a backward bifurcation at $\mathcal{R}_0 = 1$, highlighting the potential for disease persistence even when $\mathcal{R}_0$ is below unity and underscoring the complexity of TB dynamics. The presence of this backward bifurcation aligns with findings from other researchers, such as [16, 17].

Sensitivity analysis identified critical parameters – such as infection rates of immune cells, immune response efficacy, and monocyte recruitment rates – that significantly influence $\mathcal{R}_0$ and, consequently, the infection outcome. These findings emphasize the importance of targeting specific immune pathways and cellular interactions for therapeutic intervention. Simulation results demonstrated that increasing immune response strength, particularly bacterial clearance rates, markedly reduces bacterial load and infected cell populations. Conversely, higher infection rates of immune cells facilitate rapid disease progression, highlighting the need for strategies that limit bacterial invasion and replication.

The formulation of an optimal control problem enabled exploration of potential benefits from combination therapies. Numerical simulations showed that optimized treatment strategies – represented as control functions modeling drug efficacy – can substantially reduce bacterial burden and infected cell populations. Higher bounds on control efforts lead to quicker eradication of Mtb, suggesting that intensified treatment regimens, when feasible, can accelerate disease clearance. However, even with optimal control, complete

eradication within typical treatment durations remains challenging, indicating the necessity for sustained or adjunct therapies.

5.1. Concluding remarks

These mathematical insights address key questions regarding TB persistence and control. The identification of a backward bifurcation demonstrates that reducing $\mathcal{R}_0$ below one may not suffice for disease eradication within the host, paralleling challenges at the population level where transmission control alone may not eliminate endemic TB. Sensitivity analyses highlight the importance of immune response modulation, informing vaccine development and immunotherapy strategies. The results from optimal control support the implementation of combined and intensified treatment approaches, emphasizing that overcoming biological thresholds is essential for successful eradication. This modeling approach offers valuable guidance for designing effective interventions and understanding biological thresholds that sustain TB infection at both within-host and population scales.

5.2. Limitations

Despite the strengths of our approach, several limitations warrant acknowledgment. First, the model simplifies the multifaceted immune response by focusing primarily on monocytes, macrophages, and T cells, omitting other relevant immune components such as dendritic cells, neutrophils, and cytokine networks, which may influence disease progression. Second, parameter estimation relies heavily on literature values and assumptions, and variability across individuals or disease states could affect the model's predictive accuracy. Third, the model assumes homogeneous mixing within the lung environment, neglecting spatial heterogeneities that can impact infection dynamics. Fourth, the optimal control formulation considers only two control variables and does not account for potential toxicity or side effects associated with intensified therapies. Lastly, the study does not incorporate stochastic effects or the impact of immune memory, which are relevant in real biological systems.

In future work, extending the model to include spatial dynamics, additional immune components, and stochastic effects could provide a more realistic representation of TB within-host progression. Incorporating patient-specific data and exploring multi-objective optimization approaches could further enhance the clinical relevance of the findings. Despite these limitations, our results offer a foundational quantitative framework that can inform the development of more effective and personalized TB treatments.

Acknowledgments

The authors are grateful to their respective institutions for the non-financial support provided during the course of this study. The views, opinions, assumptions, or any other information expressed in this article are solely those of the authors.

Author contributions

CRediT: **Mlyashimbi Helikumi:** Conceptualization, Formal analysis, Investigation, Methodology, Software, Writing – original draft; **Steady Mushayabasa:** Conceptualization, Formal analysis, Investigation, Methodology, Software, Supervision, Writing – review & editing

Data availability statement

All data generated or analyzed during this study are included within the article. Most of the datasets are presented visually in the form of figures and graphs.

Disclosure statement

No potential conflict of interest was reported by the author(s).

Funding

This research received no specific grant from any funding agency in the public, commercial, or not-for-profit sectors.

Declaration of generative AI and AI-assisted technologies in the writing process

During the preparation of this work, the authors used chatGPT in order to optimize conciseness and clarity of text pieces. After using this tool, the authors reviewed and edited the content as needed and take full responsibility for the content of the published article.

Consent to publish

The authors declare that they have given their consent for the publication of this manuscript in Infection, Genetics and Evolution, and no third-party permissions are required.

ORCID

Mlyashimbi Helikumi http://orcid.org/0000-0002-8109-324X
Steady Mushayabasa https://orcid.org/0000-0002-7423-2934

References

[1] Jiang F, Li X, Qiao Q, et al. Global, regional, and national burden of tuberculosis, 1990–2050: a systematic comparative analysis based on retrospective cross-sectional of GBD 2021 and WHO surveillance systems. Int J Surg. 2026;112(1):250–269. doi: 10.1097/JS9.0000000000003412
[2] World Health Organization. https://www.who.int/news-room/fact-sheets/detail/tuberculosis#::text = Globally%2C%20TB%20is%20the%20world's,deaths%20related%20to%20antimicrobial%20resistance.
[3] Afriyie-Asante A, Dabla A, Dagenais A, et al. Mycobacterium tuberculosis exploits focal adhesion kinase to induce necrotic cell death and inhibit reactive oxygen species production. Front Immunol. 2021;12:742370. doi: 10.3389/fimmu.2021.742370
[4] Mohareer K, Asalla S, Banerjee S. Cell death at the cross roads of host-pathogen interaction in mycobacterium tuberculosis infection. Tuberculosis. 2018;113:99–121. doi: 10.1016/j.tube.2018.09.007
[5] Behar SM, Divangahi M, Remold HG. Evasion of innate immunity by mycobacterium tuberculosis: is death an exit strategy? Nat Rev Microbiol. 2010;8(9):668–674. doi: 10.1038/nrmicro2387
[6] Wigginton JE, Kirschner D. A model to predict cell-mediated immune regulatory mechanisms during human infection with *Mycobacterium tuberculosis*. J Immunol. 2001;166(3):1951–1967. doi: 10.4049/jimmunol.166.3.1951
[7] Marino S, Kirschner DE. The human immune response to Mycobacterium tuberculosis in lung and lymph node. J Theor Biol. 2004;227(4):463–486. doi: 10.1016/j.jtbi.2003.11.023
[8] Gammack D, Ganguli S, Marino S, et al. Understanding the immune response in tuberculosis using different mathematical models and biological scales. Multiscale Model Simul. 2005;3(2):312–345. doi: 10.1137/040603127
[9] Pedruzzi G, Rao KVS, Chatterjee S. Mathematical model of mycobacterium–host interaction describes physiology of persistence. J Theor Biol. 2015;376:105–117. doi: 10.1016/j.jtbi.2015.03.031
[10] Segovia-Juarez JL, Ganguli S, Kirschner D. Identifying control mechanisms of granuloma formation during M. tuberculosis infection using an agent-based model. J Theor Biol. 2004;231(3):357–376. doi: 10.1016/j.jtbi.2004.06.031
[11] Magombedze G, Garira W, Mwenje E. Modelling the human immune response mechanisms to *Mycobacterium tuberculosis* infection in the lungs. Math Biosci Eng. 2006;3(4):661–682. doi: 10.3934/mbe.2006.3.661
[12] Kirschner D. Dynamics of co-infection with *M. tuberculosis* and HIV-1. Theor Popul Biol. 2001;55(1):94–109. doi: 10.1006/tpbi.1998.1382
[13] Day J, Friedman A, Schlesinger LS. Modeling the immune rheostat of macrophages in the lung in response to infection. Proc Natl Acad Sci. 2009;106(27):11246–11251. doi: 10.1073/pnas.0904846106
[14] Ray JCJ, Flynn JL, Kirschner DE. Synergy between individual TNF-dependent functions determines granuloma performance for controlling Mycobacterium tuberculosis infection. J Immunol. 2009;182(6):3706–3717. doi: 10.4049/jimmunol.0802297
[15] Pienaar E, Lerm M. A mathematical model of the initial interaction between Mycobacterium tuberculosis and macrophages. J Theor Biol. 2014;342:23–32. doi: 10.1016/j.jtbi.2013.09.029
[16] Zhang W, Ellingson L, Frascoli F, et al. An investigation of tuberculosis progression revealing the role of macrophages apoptosis via sensitivity and bifurcation analysis. J Math Biol. 2021;83(3):31. doi: 10.1007/s00285-021-01655-6
[17] Du Y, Wu J, Heffernan JM. A simple in-host model for *Mycobacterium tuberculosis* that captures all infection outcomes. Math Popul Stud. 2017;24(1):37–63. doi: 10.1080/08898480.2015.1054220

[18] Zhang W. Analysis of an in-host tuberculosis model for disease control. Appl Math Lett. 2020;99:105983. doi: 10.1016/j.aml.2019.07.014
[19] Yao M, Zhang Y, Wang W. Bifurcation analysis for an in-host *Mycobacterium tuberculosis* model. Discret Contin Dyn Syst B. 2021;26(4):1–18. doi: 10.3934/dcdsb.2020324
[20] Joslyn LR, Linderman JJ, Kirschner DE. A virtual host model of *Mycobacterium tuberculosis* infection identifies early immune events as predictive of infection outcomes. J Theor Biol. 2022;539:111042. doi: 10.1016/j.jtbi.2022.111042
[21] Flores-Garza E, Hernández-Pando R, García-Zárate I, et al. Bifurcation analysis of a tuberculosis progression model for drug target identification. Sci Rep. 2023;13:17567. doi: 10.1038/s41598-023-44569-7
[22] Helikumi M, Daudi S, Lusekelo E, et al. Optimizing combination therapy against drug resistance Mycobacterium tuberculosis: a modelling study. J Biol Phys. 2025;51(1):20. doi: 10.1007/s10867-025-09685-7
[23] Kirschner D, Pienaar E, Marino S, et al. A review of computational and mathematical modeling contributions to our understanding of *Mycobacterium tuberculosis* within-host infection and treatment. Curr Opin Syst Biol. 2017;3:170–185. doi: 10.1016/j.coisb.2017.05.014
[24] Stewart GR, Robertson BD, Young DB. Tuberculosis: a problem with persistence. Nat Rev Microbiol. 2003;1:97–105. doi: 10.1038/nrmicro749
[25] Guilliams M, Mildner A, Yona S. Developmental and functional heterogeneity of monocytes. Immunity. 2018;49(4): 595–613. doi: 10.1016/j.immuni.2018.10.005
[26] Tran HTT, Van den Bergh R, Vu TN, et al. The role of monocytes in the development of Tuberculosis-associated Immune Reconstitution Inflammatory Syndrome. Immunobiology. 2014;219(1):37–44. doi: 10.1016/j.imbio.2013.07.004
[27] T'jonck W, Bain CC. The role of monocyte-derived macrophages in the lung: it's all about context. Int J Biochem Cell Biol. 2023;159:106421. doi: 10.1016/j.biocel.2023.106421
[28] Parihar A, Eubank TD, Doseff AI. Monocytes and macrophages regulate immunity through dynamic networks of survival and cell death. J Innate Immun. 2010;2(3):204–215. doi: 10.1159/000296507
[29] Wang Y, Cao D, Liu G. Application of antimicrobial drugs in Mycobacterium tuberculosis and research progress. Microb Pathog. 2025;206:107794. doi: 10.1016/j.micpath.2025.107794
[30] Larkins-Ford J, Aldridge BB. Advances in the design of combination therapies for the treatment of tuberculosis. Expert Opin Drug Discov. 2023;18(1):83–97. doi: 10.1080/17460441.2023.2157811
[31] Tiberi S, Du Plessis N, Walzl G, et al. Tuberculosis: progress and advances in development of new drugs, treatment regimens, and host-directed therapies. Lancet Infect Dis. 2018;18(7):e183–e198. doi: 10.1016/S1473-3099(18)30110-5
[32] Ufimtseva EG, Eremeeva NI. Drug-Tolerant mycobacterium tuberculosis adopt different survival strategies in alveolar macrophages of patients with pulmonary tuberculosis. Int J Mol Sci. 2023;24(19):14942. doi: 10.3390/ijms241914942
[33] Castaño D, Barrera LF, Rojas M. Mycobacterium tuberculosis alters the differentiation of monocytes into macrophages in vitro. Cell Immunol. 2011;268(2):60–67. doi: 10.1016/j.cellimm.2011.02.006
[34] Evangelopoulos D, da Fonseca JD, Waddell SJ. Understanding anti-tuberculosis drug efficacy: rethinking bacterial populations and how we model them. Int J Infect Dis. 2015;32:76–80. doi: 10.1016/j.ijid.2014.11.028
[35] Zhuang L, Yang L, Li L, et al. *Mycobacterium tuberculosis*: immune response, biomarkers, and therapeutic intervention. MedComm. 2024;5(1):e419. https://doi.org/10.1002/mco2.419
[36] Diekmann O, Heesterbeek JAP, Roberts MG. The construction of next-generation matrices for compartmental epidemic models. J R Soc Interface. 2010;7(47):873–885. doi: 10.1098/rsif.2009.0386
[37] Van den Driessche P, Watmough J. Reproduction numbers and sub-threshold endemic equilibria for compartmental models of disease transmission. Math Biosci. 2002;180:29–48. doi: 10.1016/S0025-5564(02)00108-6
[38] Castillo-Chavez C, Feng Z, Huang W. On the computation of R_0 and its role in global stability. Mathematical approaches for emerging and reemerging infection diseases: an introduction. In: Castillo-Chavez, C, van den Driessche, P, Kirschner, D & Yakubu, A.-A, editors. The IMA volumes in mathematics and its applications. Vol. 125. New York: Springer; 2002. p. 229–250.
[39] Castillo-Chavez C, Song B. Dynamical models of tuberculosis and their applications. Math Biosci Eng. 2004;1:361–404. doi: 10.3934/mbe.2004.1.361
[40] Beck CL. Modeling and control of pharmacodynamics. Eur J Control. 2015;24:33–49. doi: 10.1016/j.ejcon.2015.04.006
[41] Bolzoni L, Bonacini E, Soresina C, et al. Time-optimal control strategies in SIR epidemic models. Math Biosci. 2017;292:86–96. doi: 10.1016/j.mbs.2017.07.011
[42] Lolika PO, Modnak C, Mushayabasa S. On the dynamics of brucellosis infection in bison population with vertical transmission and culling. Math Biosci. 2018;305:42–54. doi: 10.1016/j.mbs.2018.08.009
[43] Shen M, Xiao Y, Rong L, et al. Conflict and accord of optimal treatment strategies for HIV infection within and between hosts. Math Biosci. 2019;309:107–117. doi: 10.1016/j.mbs.2019.01.007
[44] Mapder T, Clifford S, Aaskov J, et al. A population of bang-bang switches of defective interfering particles makes within-host dynamics of dengue virus controllable. PLoS Comput Biol. 2019;15(11):e1006668. doi: 10.1371/journal.pcbi.1006668
[45] Numfor E. Optimal treatment in a multi-strain within-host model of HIV with age structure. J Math Anal Appl. 2019;480(2):123410. doi: 10.1016/j.jmaa.2019.123410
[46] Kirschner D, Pienaar E, Marino S, et al. Optimal control of the chemotherapy of HIV. J Math Biol. 1997;35:775–792. doi: 10.1007/s002850050076

[47] Ullah S, Ullah O, Khan MA, et al. Optimal control analysis of tuberculosis (TB) with vaccination and treatment. Eur Phys J Plus. 2020;135(7):602–627. doi:10.1140/epjp/s13360-020-00615-1
[48] Liliopoulos SG, Stavrakakis GS, Dimas KS. Linear and non-linear optimal control methods to determine the best chemotherapy schedule for most effectively inhibiting tumor growth. Biomedicines. 2025;13(2):315. doi: 10.3390/biomedicines13020315
[49] Sharp JA, Browning AP, Mapder T, et al. Optimal control of acute myeloid leukaemia. J Theor Biol. 2019;470:30–42. doi: 10.1016/j.jtbi.2019.03.006
[50] Lenhart S, Workman JT. Optimal control applied to biological models. Boca Raton (FL): Chapman & Hall/CRC; 2007. doi:10.1201/9781420011418
[51] Marino S, Hogue IB, Ray CJ, et al. A methodology for performing global uncertainty and sensitivity analysis in systems biology. J Theor Biol. 2008;254(1):178–196. doi: 10.1016/j.jtbi.2008.04.011
[52] Hunter M, Wang Y, Eubank T, et al. Survival of monocytes and macrophages and their role in health and disease. Front Biosci. 2009;14:4079–4102. doi:10.2741/3514